UNIVERSIDAD DE MURCIA

ESCUELA INTERNACIONAL DE DOCTORADO

Multidimensional Force Spectroscopy for Nanoscale Characterization of Electrostatic and Dispersion Interactions

Espectroscopía de Fuerzas Multidimensional para la Caracterización en la Nanoescala de las Interacciones Electrostática y de Dispersión

D. Jesús Sánchez Lacasa

2018

MULTIDIMENSIONAL FORCE SPECTROSCOPY FOR NANOSCALE CHARACTERIZATION OF ELECTROSTATIC AND DISPERSION INTERACTIONS

ESPECTROSCOPÍA DE FUERZAS MULTIDIMENSIONAL PARA LA CARACTERIZACIÓN EN LA NANOESCALA DE LAS INTERACCIONES ELECTROSTÁTICA Y DE DISPERSIÓN

Jesús Sánchez Lacasa
Dirigida por Jaime Colchero Paetz

UNIVERSIDAD DE MURCIA
October 2018

Contents

Resumen

La microscopía de fuerzas atómicas, conocida habitualmente por sus siglas en inglés, AFM (*Atomic Force Microscopy*) es una técnica ampliamente usada en diferentes campos de la ciencia por su resolución y por su gran versatilidad. El AFM es capaz de obtener imágenes de superficies, de sistemas pequeños y de átomos y moléculas adsorbidos a una escala nanométrica, atómica e incluso subatómica en medios tan dispares como el aire, líquidos y el vacío. El funcionamiento del AFM se fundamenta en la interacción entre una punta afilada, que actúa como sonda, y la muestra que queremos analizar. Para obtener las imágenes que mencionaba, esta interacción se mantiene constante cambiando la posición relativa entre la punta y la muestra en la dirección normal a la superficie mientras la punta escanea la superficie (o viceversa, según el montaje experimental) en la dirección tangente a la misma (posición lateral, plano x-y). Por otro lado, en las mediciones de espectroscopía, la posición lateral se mantiene constante mientras la posición normal de la punta varía para tener acceso a las propiedades del material a través de la interacción punta-muestra. El AFM permite no sólo obtener imágenes de la topografía de la superficie, sino también determinar otras características físicas de la misma. En particular, las técnicas AFM para estudiar propiedades electrostáticas y magnéticas son ampliamente utilizadas.

La interacción entre la punta y la muestra es el principio físico fundamental en el que se basa el funcionamiento del AFM. Es a través del análisis de esta interacción, con las técnicas y los modelos adecuados, que el AFM puede acceder a las diferentes propiedades de las muestras en las que se emplea. Son muchas, y de muy diferente naturaleza, las contribuciones a la interacción total existentes entre la punta y la muestra. Fuerzas elásticas, capilares, de dispersión, electrostáticas o magnéticas son algunas de las que suelen estar presentes en nuestros experimentos y contribuir a la interacción total efectiva entre la punta y la muestra. Unas dependen de las propiedades químicas de la punta y la muestra, otras de las propiedades mecánicas de los materiales que las formas, también las hay que depende de la geometría o de la distancia entre la punta y la muestra. Todas ellas actúan de forma conjunta y, por lo tanto, es necesario y fundamental desarrollar técnicas experimentales que sean capaces de discernir entre las diferentes contribuciones para tener acceso, de esa forma, a las propiedades que la caracterizan. Con el fin de conseguir acceso a estas propiedades de forma cada vez más cuantitativa, la comunidad de AFM sigue trabajando en el desarrollo de estas técnicas y la mejora de las ya existentes.

En este punto radica precisamente el objetivo de esta tesis. Nos proponemos

desarrollar una técnica experimental que, de forma cuantitativa, sea capaz de caracterizar dos de las contribuciones más interesantes a la interacción total entre la punta y la muestra: las interacciones electrostática y de dispersión. Una técnica así, que sea capaz de caracterizar las superficies a través de propiedades químicas como la diferencia de potencrial de contacto (CPD), la constante de Hamaker o la constante dieléctrica, dotaría al AFM de una habilidad novedosa para caracterizar e identificar químicamente las muestras en las que se emplea a escala nanométrica.

Sería imposible, sin embargo, conseguir este objetivo sin abordar previamente otras consideraciones de carácter más técnico o metodológico pero que resultan imprescindibles para lograr el objetivo principal y que se van estudiando a lo largo de los capítulos de esta tesis.

Para comenzar, es imprescindible entender cómo funciona el AFM y sus modos de operación, tanto desde el punto de vista experimental como desde el punto de vista teórico. La experiencia previa del grupo de investigación DIANA, en el que realizo esta tesis, y de sus miembros es imprescindible para este cometido. Son muchos los años y los estudios previos que se han dedicado al diseño y la implementación de las diferentes técnicas de AFM, así como a explorar los límites teóricos del mismo tanto desde el punto de vista teórico como desde el punto de vista experimental. En este contexto, es fácil situar mi trabajo como un intento más en la dirección de mejorar nuestro entendimiento de los modos de operación dinámicos del AFM. En particular los modos AM-AFM (modulado en amplitud) y FM-AFM (modulado en frecuencia).

Un primer paso, que ya se puede anticipar por lo que he mencionado previamente, consiste en modelar de forma correcta la interacción entre la punta y la muestra. Tener una visión acertada de los fenómenos físicos que ocurren entre la punta y la muestra será fundamental, tanto a la hora de proponer y desarrollar los experimentos, como a la hora de analizar cuantitativamente los resultados que estos arrojen. Por lo tanto, una parte del esfuerzo dedicado a este trabajo consistirá precisamente en identificar estos fenómenos físicos, tales como la formación de cuellos líquidos entre la punta y la muestra, y entender cómo afectan estos a la interacción y, por lo tanto, a los datos que recogemos en las medidas de AFM.

Analizar y entender estos fenómenos y sus efectos en la interacción entre la punta y la muestra, nos dará la capacidad de operar el AFM de manera más controlada, acercándonos tanto como podamos a la muestra pero evitando la formación de cuellos líquidos entre la punta y la muestra y evitando también, por lo tanto, las no linealidades asociadas a esta interacción no conservativa. Con esto en mente, distinguimos para nuestros experimentos tres modos de AFM: un modo de **no-contacto real** (*true non-contact mode*), un modo de **contacto intermitente** (*intermittent mode*) y un modo de **contacto** (*contact mode*).

Para la comunidad de AFM no hará falta indagar más en el modo de contacto puesto que resulta ser un modo usual en AFM en el que la interacción entre la punta y la muestra se caracteriza por ser de carácter mecánico. Sin embargo, puesto que creemos que aquí radica una de las contribuciones más interesantes de este trabajo y para nuestros experimentos y el análisis de los datos resulta fundamental, sí que resulta oportuno profundizar algo más en la definición de los otros dos modos, cuya distinción resulta novedosa para muchos dentro de la comunidad científica en torno al AFM en aire. Separamos así lo que tradicionalmente se conoce como modo de no contacto en dos modos con características diferentes. Como su propio nombre indica, llamamos modo de no-contacto real al modo en el que opera el AFM sin que exista ninguna tipo de contacto entre la punta y la muestra. Excluye por tanto, y esto es lo novedoso, la formación de cuellos líquidos entre la punta y la muestra. En este modo, las únicas contribuciones a la interacción entre la punta y la muestra presentes son las interacciones de van der Waals (dispersión) y electrostática. Habría que añadir la interacción magnética si la punta estuviese fabricada o recubierta de un material magnético. En cambio, llamamos modo de semi-contacto al modo en el que la formación y ruptura de cuellos líquidos entre la punta y la muestra añaden una interacción disipativa adicional al sistema.

Dada nuestra intención de mejorar en la obtención de resultados cualitativos es imprescindible tener una interacción punta-muestra bien definida y, por lo tanto, resulta necesario operar el AFM en el modo que hemos convenido llamar *de no-contacto real*. Así mismo, hemos comprobado que la técnica de espectroscopía en FM-AFM es la adecuada para obtener los mejores resultados en aire.

Para el empleo de esta técnica de caracterización de las interacciones electrostática y de dispersión ha sido imprescindible el uso de una técnica previa llamada *imágenes de interacción*, que consiste en registrar con el AFM la interacción en un punto de la muestra a medida que se varía la distancia entre punta y muestra y la diferencia de potencial eléctrico aplicado entre ambas.

Para acabar con la metodología, es necesario desarrollar un programa que se encargue de las particularidades del análisis de los datos obtenidos mediante esta técnica y su posterior procesado y representación para la obtención de resultados cuantitativos.

Haciendo uso de esta nueva técnica de caracterización de la interacción entre la punta y la muestra, en este trabajo somos capaces de reconstruir de forma precisa la interacción electrostática y la de dispersión (van der Waals) y obtener de ellas propiedades características de los materiales como el CPD. De la comparación de ambas interacciones conseguimos además evitar la dependencia con la geometría de la punta (que normalmente se desconoce) y calcular la constante de Hamaker (que modela la interacción de dispersión) y la posición real de la superficie con respecto a la punta (en las técnicas habituales sólo se conocen posiciones relativas). Aplicamos esta técnica en dos experimentos diferentes: uno en el que tratamos de diferenciar entre diferentes sustratos formados por diferentes metales y otro en el que empleamos esta técnica para caracterizar el grado de contaminación de las puntas de AFM que utilizamos en los experimentos al aire. Ambos experimentos con interesantes conclusiones.

Una deficiencia del AFM con respecto a su técnica hermana, el microscopio de efecto túnel (STM, *Scanning tunneling microscopy*), es la dificultad de caracterizar químicamente de forma cualitativa las muestras. En este primer experimento, utilizamos como muestras tres sustratos conductores diferentes: oro (Au), platino

(Pt) y grafito (HOPG, *highly oriented pyrolytic graphite*). En ellos aplicamos la técnica descrita anteriormente y calculamos tanto el CPD que los caracteriza como la constante de Hamaker, encontrando valores reproducibles y diferencias entre los distintos materiales lo suficientemente significativas como para distinguir entre ellos. En particular, encontramos que una representación conjunta de ambas propiedades proporciona una capacidad novedosa hasta ahora de clasificar e identificar materiales.

Una punta estable y bien definida es esencial para una adquisición de datos fiable. Es bien sabido que la resolución de las imágenes y, de manera general, la calidad de los datos medidos dependen de forma crítica de la geometría de la punta tanto como de las propiedades del material que la forma. En consecuencia, numerosos esfuerzos se han dedicado a la fabricación de puntas bien caracterizadas y tan afiladas como las técnicas de fabricación lo permitan. Por otro lado, es importante resaltar que incluso la punta mejor fabricada puede tener un uso limitado si no se mantienen las propiedades especificadas durante el funcionamiento del AFM y la toma de imágenes. Para este segundo experimento, asumimos que el nivel de contaminación de la punta es similar al de la micropalanca a la que pertenece y estudiamos tres micropalancas con diferentes grados de contaminación: una expuesta a la contaminación durante mucho tiempo, otra de una caja de puntas recién abierta y otra que hemos limpiado a conciencia usando un método conocido como RCA, en el que pasa por dos disoluciones, una de carácter básico y otra de carácter ácido. Estos tres sustratos se estudian con la técnica aquí descrita y, adicionalmente, con la técnica de microscopía de sonda Kelvin (KPFM). De este trabajo se concluye que no sólo la contaminación en la punta, si no que a veces también en la muestra, es difícil de visualizar y de detectar. Pero es, sin embargo, muy importante y determina significativamente los resultados de AFM y su interpretación. Además, este método permite una caracterización simple, efectiva e *in-situ* del sistema punta-muestra sin necesidad de sacar ni la punta ni la muestra del montaje experimental del AFM.

Para acabar, llegamos a las conclusiones de que en este trabajo que se presenta, se ha desarrollado y aplicado una técnica de espectroscopía de fuerza avanzada para obtener propiedades específicas de los materiales. Con esta técnica es posible distinguir y caracterizar de forma precisa las interacciones electrostática y de dispersión además de obtener propiedades relativas a los materiales tales como el CPD o la constante de Hamaker. Por lo tanto, aplicando esta técnica, es posible caracterizar superficies metálicas y semiconductoras usando la constante de Hamaker y el CPD.

Además, el desarrollo de esta técnica ha supuesto, de forma paralela un avance en el entendimiento de la interacción entre la punta y la muestra en AFM que ha conducido a una reclasificación de los modos de medida que creemos que será importante tener en cuenta para avanzar en la obtención de resultados cualitativos con las técnicas de AFM. Con este mismo fin, se ha visto y demostrado que es importante tener superficies bien definidas al aire y que la contaminación es un factor a tener en cuanta a la hora de interpretar los resultados.

Summary

Atomic Force Microscopy (AFM) is a technique widely used in different fields of science due to its resolution and great versatility. The AFM allows to obtaining images of surfaces, small systems and atoms and molecules adsorbed at a nanometric, atomic and even subatomic scales in environments as different as air, liquids and vacuum. The operation of AFM is based on the interaction between a sharp tip acting as a probe and the sample we want to analyze. To obtain images, this interaction is kept constant by changing the relative position between the tip and the sample in the normal direction to the surface while the tip scans the surface (or the contrary, depending on the experimental set-up) in the direction tangent to the surface (lateral position, x-y plane). In spectroscopy measurements, the lateral position is kept at a fixed point while the vertical separation of the tip is varied to access the properties of the material through the tip-sample interaction. The AFM allows not only to obtain images of the topography of the surface, but also to determine other physical characteristics of the surface. In particular, AFM techniques to study electrostatic and magnetic properties are widely used.

The interaction between the tip and the sample is the fundamental physical principle on which the operation of AFM is based. It is through the analysis of this interaction, with the appropriate techniques and models, that AFM can access the different properties of samples. There are many, and of a very different nature, contributions to the total interaction between the tip and the sample. Elastic, capillary, dispersion, electrostatic or magnetic forces are some of the ones that are usually present in our experiments and contribute to the total effective interaction between the tip and the sample. Some depend on the chemical properties of the tip and the sample, others on the mechanical properties of the materials and most depend on the geometry and the distance between the tip and the sample. All of them act together and, therefore, it is necessary and fundamental to develop experimental techniques that are capable of discerning between the different contributions in order to have access to the properties that characterize it. In order to gain access to these properties in an increasingly quantitative manner, the AFM community continues to work on the development of these techniques and the improvement of existing ones.

This is precisely the aim of this thesis. We propose to develop an experimental technique that, quantitatively, is capable of characterizing two of the most interesting contributions to the total interaction between the tip and the sample: electrostatic and dispersion interactions. Such a technique, which is capable of

characterizing surfaces through chemical properties such as contact potential difference (CPD), Hamaker constant or dielectric constant, would give AFM a novel ability to characterize systems at the nanoscale and chemically identify the samples analysed.

It would be impossible, however, to achieve this objective without first addressing other considerations of a more technical or methodological nature but which are essential to achieve the main objective.

To begin with, it is essential to understand how AFM works and its modes of operation, both experimentally and theoretically. The previous experience of the DIANA research group, in which I write this thesis, and of its members is essential for this task. Many years and previous studies have been devoted to the design and implementation of different AFM techniques, as well as to exploring the theoretical limits of AFM from both a theoretical and an experimental point of view. In this context, it is easy to situate my work as one more attempt in the direction of improving our understanding of the dynamic modes of operation of the AFM. In particular AM-AFM (amplitude modulated) and FM-AFM (frequency modulated) modes.

A first step, which can already be anticipated by what has been previously mentioned, is to correctly modeling the interaction between the tip and the sample. Having an accurate vision of the physical phenomena that occur between the tip and the sample will be fundamental; both, when proposing and developing experiments, as well as when analyzing quantitatively the results they produce. Therefore, part of the effort in this thesis will be focus on precisely identifying these physical phenomena, such as the formation of capillary bridges between the tip and the sample, and understanding how these affect the interaction and, therefore, the data we register in the AFM measurements.

Analyzing and understanding these phenomena and their effects on the interaction between the tip and the sample will give us the ability to operate the AFM in a more controlled manner, getting as close as we can to the sample but avoiding the formation of liquid necks between the tip and the sample and also avoiding, therefore, the non-linearity associated with this non-conservative interaction. With this in mind, we distinguish for our experiments three modes in AFM: a **true non-contact** mode, a **intermittent contact mode** and a **contact mode**.

For the AFM community it will not be necessary to further investigate the contact mode since it turns out to be a usual AFM mode in which the interaction between the tip and the sample is characterized by being mechanical in nature. However, since we believe that this is one of the most interesting contributions of this work and for our experiments and the analysis of the data is fundamental, it is appropriate to discuss further the definition of the other two modes since their distinction is most probably less clear for many in the scientific community around AFM in air. We thus separate what is traditionally known as the non-contact (attractive) mode into two modes with different characteristics. As the name implies, we call **true non-contact** mode to the one in which the AFM operates without any contact between the tip and the sample. It excludes therefore, and this is the novelty, the formation of liquid necks between the tip and the sample. In this mode, the only contributions to the interaction between the tip and the sample present are the van der Waals (dispersion) and electrostatic interactions. Magnetic interaction would have to be added if the tip was made of or covered with a magnetic material. We will denominate **intermittent contact** mode the regie where the formation and break of capillary bridges between the tip and the sample add additional dissipative interaction to the system.

Given our intention to improve the achievement of qualitative results, it is essential to have a well-defined tip-sample interaction and, therefore, it is necessary to operate the AFM in the way we call true non-contact. Also, we have verified that the technique of spectroscopy in FM-AFM is the best mode to obtain high quality spectroscopy results in air.

For the use of this technique of characterization of electrostatic and dispersion interactions has been essential the use of a previous technique called *interaction images*, which consists of recording with the AFM the interaction at a point of the sample as the distance between tip and sample and the difference in applied voltage between the two varies.

Finally, with regard to the methodology developed during this thesis, it has been necessary to develop a postdata acquisition tool to automatically the wealth of data contained in the different channels that are acquired in a typical 2-dimensional interaction image. This program is in charge of the particularities of the analysis of the data obtained by means of this technique and its subsequent processing and representation in order to obtain quantitative results.

Making use of this new technique of characterization of the interaction between the tip and the sample, in this work we are able to reconstruct in a precise way the electrostatic and the dispersion (van der Waals) interactions, and to obtain from them characteristic properties of materials such as CPD. By comparing the two interactions, we can also avoid dependence on the geometry of the tip (which is normally unknown) and calculate the Hamaker constant (which models the dispersion interaction) and the real position of the surface with respect to the tip (in the usual techniques only the relative positions are known). We apply this technique to address two important issues in AFM: on the one hand we try to differentiate between samples formed by different metals and on the other, we use this technique to characterize the degree of contamination of the AFM tips used in our experiments. Both experiments yield very interesting conclusions.

A deficiency of AFM with respect to its related technique, the STM (*Scanning tunneling microscopy*), is the difficulty to chemically characterize the samples in a quantitative way. In this context, in this thesis, three different conductive substrates as samples: gold (Au), platinum (Pt) and graphite (HOPG, *highly oriented pyrolytic graphite*) have been used as model samples to try a quantitative chemical characterization. On these samples the technique described above has been used to calculate both the CPD that characterizes them and the Hamaker constant, finding reproducible values and differences between the different materials significant enough to distinguish between them. In particular, we find that a joint representation of both properties provides a powerful and novel scheme to classify and identify materials on the nanoscale.

A stable, well-defined tip is essential for reliable data acquisition. It is well known that the resolution of images and, in general, the quality of measured data depend critically on the geometry of the tip as well as on the properties of its material. As a result, many efforts have been devoted to the manufacture of well-characterized tips and as sharp as manufacturing techniques allow. On the other hand, it is important to note that even the best manufactured tip can have limited use if the specified properties are not maintained during AFM operation and imaging. To address this issue in this thesis, we assume that the level of contamination of the tip is similar to that of the cantilever to which it belongs and have studied three cantilevers with different degrees of contamination: one exposed to contamination for a long time, another taken from a newly opened tip box and a third that had been consciously cleaned using a method known as RCA, where the sample to be cleaned is passed through two solutions, one basic and another one acid. These three substrates are studied with the technique described here and, additionally, with Kelvin probe microscopy (KPFM). From this experiments we conclude that not only the contamination on the tip, but sometimes also that on the sample is difficult to visualize and detect, but is, nevertheless, very important and determines significantly the results of AFM and its interpretation. In addition, this method allows a simple, effective and *in-situ* characterization of the tip-sample system without the need to remove either the tip or the sample from the experimental AFM set-up.

Summarizing, in this study, an advanced force spectroscopy technique has been developed and applied to obtain specific material properties of tip and sample. With this technique it is possible to accurately distinguish and characterize electrostatic and dispersion interactions as well as to obtain material-related properties such as CPD or the Hamaker constant of the tip-sample system. Therefore, by applying this technique, it is possible to characterize metal and semiconductor surfaces using the Hamaker constant and the CPD.

In addition, the development of this technique has meant, in parallel, an advance for the understanding of the interaction between the tip and the sample in AFM that has led to a reclassification of the measurement modes. The disstinction between true-non contact and intermittent contact will be important to take into account for improving AFM, since quantitative results can in many circumstances only be obtained in the tre non-contact regime. With this same purpose, it has been seen and demonstrated that it is important to have well-defined surfaces in air and that pollution is an important factor to take into account when interpreting results.

Chapter 1

Fundamentals of Atomic Force Microscopy

1.1 The origin of atomic force microscopy

The invention of the scanning tunneling microscope (STM) [1] by Binnig and Rohrer *et al.* in 1981 meant the ability to image atoms in real space for the first time ever and was therefore a huge step forward in surface science.

In a very simplified description, STM is based on a very sharp metallic tip (Fig. 1.1a) mounted on a very precise scanning device. All of it is controlled within a low noise electronic system. This set-up is able to measure the tunneling current between atoms on the surface and the sharp tip with subatomic resolution.

Rapidly STM allowed to solve some of the most intriguing problems in surface physics by then—e.g., the structure of Si(111)(7x7) [2], Au(100) [3] and Ni(110) [4] surfaces, among others. Contribution to science was considered so important that G. Binnig and H. Rohrer were awarded with the Nobel Prize in Physics in 1986, shared with E. Ruska for the design of the first electron microscope.

But what about the atomic force microscope or atomic force microscopy (AFM) so far? The invention of the AFM cannot be separeted from the STM itself. During the first years investigating with the STM it was noticed that some forces were acting between the tip and the sample [5] when the distance between them was close enough for the tunneling current to flow. The first prototype AFM came in 1986 [6] and the tunneling tip had been replaced by a force-sensing cantilever with a sharp tip attached at the end of it (Fig. 1.1b) that probes the sample.

1.2 Tip-sample interaction within AFM

Tip-sample interaction is the basic physical principle on which the AFM is based. Using the interaction between the tip and the sample, the AFM is able to probe surfaces in the nanoscale. Generally, interaction can be represented by an energy field $W(x, y, z)$ which describes the energy of the tip when the tip is positioned at

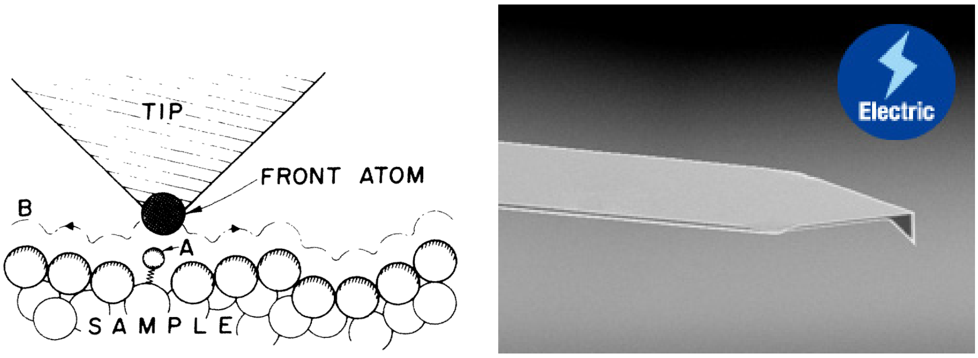

(a) STM or AFM tip close to a surface. The tip follows the line B either keeping tunelling current constant in STM or force constant in AFM in order to map the surface. Figure seen at Binnig et al. (1986) for the description of the principle opearation of an STM or AFM.

(b) AFM replaces de STM's tip by a force-sensing cantilever ended with a sharp tip that probes the sample.

Figure 1.1

the location (x, y, z). AFM allows to obtain, for a distance d between the tip and the sample, the force acting between the tip and the sample due to that interaction

$$F(x, y; d) = -\frac{\partial W}{\partial z}(x, y, z)\bigg|_{z=d}. \tag{1.1}$$

This expression reflects how, from a three-dimensional magnitude $W(x, y, z)$, a two-dimensional map of the interaction at a given distance between the tip and the sample can be obtained, $F(x, y; d)$.

1.2.1 Relevant tip-sample interactions in AFM

There are many, and of a different nature, contributions to the total interaction between the tip and the sample. It will be part of the experimental techniques described in this work to discern among them. Some of the most relevant interactions found in AFM will be described below.

Elastic forces

When tip and sample are in contact, an elastic interaction occurs between the surfaces in contact. Hertz's theory [7, 8] offers a model for this type of interactions. Consider that the radius of the contact surfaces are R and R' and that, as a result of the forces applied, the bodies compress and indent a distance h. The relationship between the applied force F and the deformation h is then given by,

$$F = h^{3/2}\frac{3D}{5}\sqrt{\frac{RR'}{R+R'}}, \tag{1.2}$$

where D is a constant that depends on the elastic properties of the surfaces. Specifically, D, depends on Poisson's module σ and Young's module E,

$$\frac{1}{D} = \frac{3}{4}\left(\frac{1-\sigma^2}{E} + \frac{1-\sigma'^2}{E'}\right). \tag{1.3}$$

Capillary forces

When the AFM is operated in air a capillary bridge is created between the tip and the sample when they are close enough—around 4-5 nm. This phenomena is the origin of this interaction also called *adhesion force* and it depends strongly on the relative humidity[9].

Van der Waals forces

Its origin lays on the interaction between dipoles and induced dipoles in atoms and both neutral and polar molecules. It has three different contributions, all of them with the same dependence on the inverse sixth power of the distance.

- **Dispersion interaction.** The only one out of the three components that is always present since it acts between neutral atoms and molecules—even chemically inert noble gas atoms are affected by dispersion forces—and hence, the most important contribution to the total Van der Waals interaction in most of the cases. The time averaged dipole moment of any neutral atom or molecule is zero. However, at any instant there exists a finite dipole moment because of the instantaneous position of its electrons. This instantaneous dipole creates and electric field that is able to polarize any nearby neutral atom or molecule. Dispersion forces are long range forces, they are effective from distances greater than $10-20\ nm$ down to interatomic spacings around $0.2\ nm$. They can be repulsive or attractive and do not follow a simple power law. They bring molecules together but also play a roll aligning and orienting them. Finally, dispersion forces are not additive since the presence of a third molecule perturbs the polarization state of the original ones and the result is not as simple as adding the interactions by pairs. However, additivity is usually assumed in order to simplify the integration of the interaction in macroscopic bodies.

- **Induction interaction.** Also called *Debye interaction*. It is the result of the interaction between a polar molecule and the dipole that its presence induces on any other neutral atom or molecule nearby.

- **Orientation interaction.** Also called *Keesom interaction*. It has its origin in the interaction between two polar molecules and its effect consists on averaging the angle between dipoles.

For a sphere with radii R and a flat surface separated a distance d, the Van der Waals interaction energy is given by

$$W(d) = -\frac{AR}{6d} \tag{1.4}$$

and so, the force acting between them is

$$F(d) = -\frac{AR}{6d^2}, \tag{1.5}$$

where A is the Hamaker constant [10] that models the van der Waals interaction for macroscopic bodies and it is dependent on the properties of the materials that the tip and the sample are made of as well as on the medium between them (see chapter 2).

Magnetic forces

Magnetic forces are only present in AFM when both tip and sample have magnetic properties. For simplicity, the tip is usually considered to behave as a magnetic dipole and the sample is magnetic, the force between tip and sample can be expressed as followed

$$\mathbf{F} = \mu_0(\mathbf{m}\cdot\nabla)\mathbf{H}, \tag{1.6}$$

where μ_0 is the permeability of vaccum, $\mathbf{m}$ is the magnetic moment of the tip and $\mathbf{H}$, the magnetic stray field. The AFM technique which is used to study the magnetic properties of the sample based on this principle is called **magnetic force microscopy (MFM)** [11]. MFM has been proved to be useful in the study of magnetic domains [12, 13], single vortices in superconducting materials [14] as well as the effects of magnetic dissipation [15].

Electrostatic forces

Electrostatic forces in AFM are originated by the presence of an electrostatic field between the tip and the sample. The origin of the electrostatic field can be diverse. Localized charges on insultating tips and sample generates an electric field that originates an electrostatic force between them. This force obeys the Coulomb's law. On the other hand, electrostatic forces also act between conductive tip and a sample when they are at a different potencial. If the tip-sample system is considered as a capacitor with distance-dependence capacitance C, the force is given by

$$F_{estat}(d) = \frac{\partial C(d)}{\partial d}(U_{bias} - U_{CP})^2 \tag{1.7}$$

where U_{bias} is the bias voltage applied between tip and sample and U_{CP} is the contact potencial difference due to the different work functions of tip and sample[16]. The term $\frac{\partial C}{\partial z}$ depends on the tip geometry. For a tip modeled as a truncated cone and a half sphere with radii R [17] and considering small distances between tip and sample, the expresion 1.7 turns into

$$F_{estat} = \pi\epsilon_0 \frac{R}{z}(U_{bias} - U_{CP})^2. \tag{1.8}$$

The AFM technique that is able to study the electrosatic properties of the sample by using this concepts above is usually refered as **electrostatic atomic force microscopy (EAFM)**.

1.3 Experimental set-up

1.3.1 The PID controller

A proportional-integral-derivative controller[18] (PID controller or three term controller) is a control loop feedback mechanism widely used in industrial control systems and a variety of other applications requiring continuous real-time control. A PID controller continuously calculates an error value $e(t) = X(t) - X_{SP}$ as the difference between a desired setpoint (X_{SP}) and a measured process variable X and applies a correction based on proportional, integral, and derivative terms (denoted P, I, and D respectively) of the error signal $e(t)$, hence the name.

1.3.2 Lock-in amplifier

The lock-in amplifier [19] uses a known wave carrier signal to extract another signal from a very noisy environment. It is fundamental in the use of every AFM techniques where the signal from the tip-sample interaction may be so low that is usually hidden behind thermal or electrical noise. In addition, it is used phase-sensitive detection of the cantilever motion in dynamic AFM experiments.

The basic principles of the technique lays in the orthogonality of the sinusoidal functions. In AFM, the lock-in amplifier takes an input signal—the deflection of the cantilever as registered by the detection system—$U_0 \cos(\omega_0 t)$ and it multiplies the input signal by a reference signal $U_{ref} \cos(\omega_{ref} t)$. The result of this product is averaged over a time interval (time constant of the PLL detection) such that it exceeds the period of both signals. When $\omega_0 \neq \omega_{ref}$, the average is null, but if $\omega_0 = \omega_{ref}$, the average results in $U_0 U_{ref}/2$. Therefore, since U_{ref} is known, we can determine the value of U_0, the signal of interest. In this way, any contribution to the signal to be investigated that is not at the reference frequency will be attenuated. It should be noted that in this process the phase difference between the two signals must adjusted so that it is null.

For convenience, in AFM, the so-called two-phase lock-in amplifier[20] is used. It does the same calculation as before but it uses an additional reference signal that is 90° shifted in phase.

The lock-in technique can be interpreted from a more general point of view. Taking the original signal as ω and the reference signal as ω_{ref}, their product results in signals with $\omega - \omega_{ref}$ and $\omega + \omega_{ref}$. Therefore, the lock-in technique allows us to see signals in the window corresponding to the bandwidth.

1.3.3 Phase-locked loop

The **phase-locked loop (PLL)** is a control system that generates an output signal whose phase is related to the phase of an input signal.

1.4 Operation modes in AFM: static and dynamic

Many modes of operation have been described in AFM. These operational modes can be divided into **static** and **dynamic** modes depending on whether the static bending of the cantilever or its oscillating properties are measured, respectively. Often, they can also be distinguished according to whether the tip is in **contact** with the sample or it is not. Note that these distinctions are not equal, even though usually contact mode AFM is performed statically and non-contact mode is implemented statically. Actually, contact mode is some times performed dynamically at—or near—a contact resonance to avoid the problem due to drift at F_N.

Most of the work in the thesis will be measured taking advantage of possibilities of the dynamic mode in the non-contact regime.

1.4.1 Static modes

AFM static modes can be operated either in contact or non-contact. However, from an historic point of view, the most used static mode is the so-called **contact-static mode**[1] in which the cantilever bending is kept constant by changing the piezo z-position. As a result, a topographic image at constant force is recorded.

It is also possible to scan the sample at a **constant height** (non-contact) above the sample while recording the deflection of the cantilever. This other mode results in a map of the force suffered by the cantilever. This mode is used when working with long range forces such as magnetic or electrostatic as well as in experiments in aquous enviroments, otherwise capillary bridges and jump-to-contact makes it very difficult to work properly in air.

1.4.2 Dynamic modes

In the dynamic modes, the cantilever is vibrated and changes on the oscillation properties of the cantilever—due to tip-sample interaction—are measured. These

---

[1] This mode is sometimes simple and ambiguously named **contact mode**, which—in my opinion—leads to a misunderstanding since it assumes that the only possible contact mode is operated statically while some recent works try to take advantage of oscillating the cantilever while in contact with sample in order to study the machanical properties of the sample.

properties include the oscillation amplitude, the resonance frequency or the phase between excitation driving force and oscillation of the cantilever. **Dynamic modes [21] are named after the signal used as a feedback parameter in order to control the tip-sample distance and track the topography of the sample surface.**

AM-AFM

Amplitud modulated dynamic scanning force microscopy (AM-AFM) is the mode where the oscillating amplitude is maintained constant by changing the tip-sample distance within the feedback controller. Most of the experiments in air are preformed using this mode. Besides the topography, other material properties can be mapped withing this mode if the phase shift between the driving signal and the deflection signal is recorded as it comes from the lock-in amplifier (sec. 1.3.2).

PhM-AFM

The **phase modulated dynamic scanning force microscopy (PhM-AFM)** mode is that in which the phase shift between the excitacion and the deflection signals is used as a parameter for the feedback controller in order to obtain a map of the topography of the sample.

FM-AFM

The **frequency modulated dynamic scanning force microscopy (FM-AFM)** was first introduced by Albrecht *et al.* [22], who had demonstrated that it was possible to increase the sensitivity of the AFM using this mode by operating in a moderate vacuum, where the Q-factor of the oscillating cantilever was considerably increased.

The set-up for FM-AFM requires an additional controller which is able to obtain the resonance frequency of the system from the phase shift signal that comes out from the lock-in amplifier. This controller is an FM demodulator and the most used nowadays is the one based on the PLL principle reviewed on section 1.3.3, which is basically in charge of keeping the system on its resonance frequency by fixing the phase shift equal to 90°. Then the frequency shift signal is used as a parameter for the feedback that maps the topography as it happens on the previous modes.

FM-AFM is the mode par excellence when the AFM is operated in vacuum for atomic resolution [23, 24, 25]. FM-AFM can also be used in air and liquids [26, 27, 28] to achive a true non-contact regime and atomic resolution with good results.

In particular, this mode is also used in this thesis to obtain images in the true non-contact regime (see section 2.3).

1.5 Spectroscopic techniques

AFM versatility is well known, many useful AFM-based techniques have been developed since its invention. In this section I will explain briefly the basic ones for the work in this thesis.

1.5.1 Force vs. distance curves

Force-distance curves are one of the easiest measurements that can be performed in AFM to extract information about the tip-sample interaction. It is based on fixing the lateral position of the tip over the sample and acquiring the normal force (F_N) acting on the cantilever while varying the tip-sample distance. Therefore, very simple signal processing is needed as well as scanning the sample is not required.

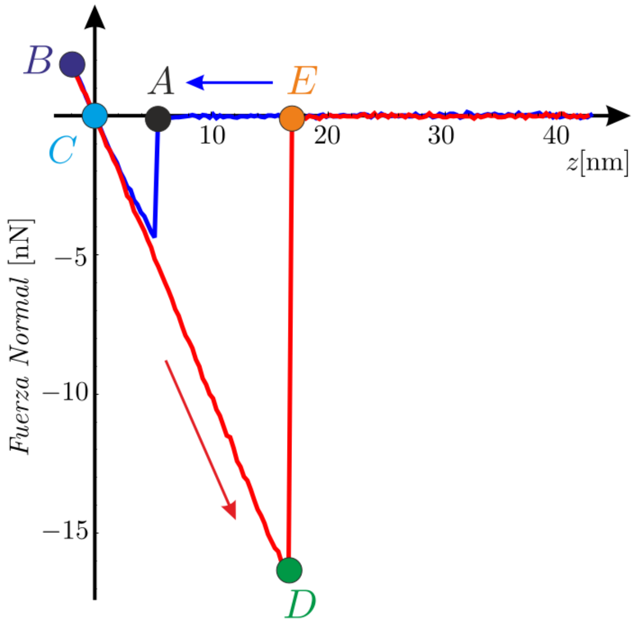

Figure 1.2: Example of a usual force vs. distance curve where interesting points have been labeled, see main text.

In figure 1.2 an experimental $F(z)$ curve is shown corresponding to a full cycle in air approaching to and withdrawing from the sample: the tip starts from a certain distance, it approaches to the sample until tip and sample are in contact and then the tip-sample distance is again increased all the way back to the original position. While approaching, normal force is approximately constant until it reaches point A, where the jump to contact occurs. From the physical point of view, the jump to contact is the result of the normal force second derivative being greater than the spring constant, c_{lever}, of the cantilever—in air, it happens because a capillary bridge is formed between the tip and the sample that brings them together[29, 30]. After the contact point, the cantilever is bent as we keep approaching. The

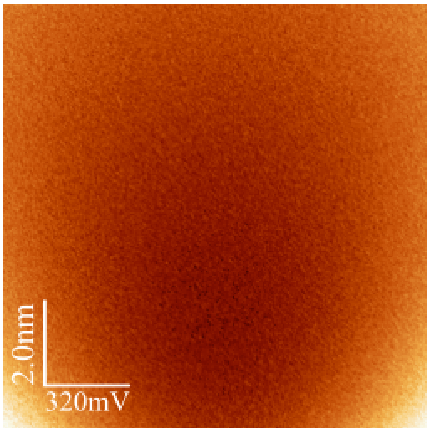

Figure 1.3: Example of an usual frequency interaction image where tip-sample distance is varied in the vertical axis (slow scan) and the applied voltages in the horizontal axis (fast scan).

normal force in this case is proportional to the deflection of the cantilever, while the deflection of the cantilever is equal to the z-piezo displacement if we assume that there is no deformation of the sample—this is usually true for non-biological samples for the contact region since the cantilever is usually softer than the sample, therefore, $F(z) = c_{lever}z$. At point B—where greatest force is applied—the sense of the movement is reversed and the deflection of the cantilever is relaxed linearly until point C. From point C to D, adhesion and capillary forces prevent the tip from separating from the sample and cause the cantilever to deform in the opposite way. At point D, the deflection of the cantilever has enough potential energy to make it escape the adhesion and capillary forces on the sample surface. Then, after oscillating freely for some cycles, the cantilever comes back to its equilibrium point where normal force is zero.

Some useful information about the tip-sample system can be extracted from the force vs. distance curve. The **adhesion force** is the difference in force between points D and E. In air, this adhesion force is originated by the formation of a capillary bridge between the tip and the sample as I mentioned earlier so it depends on the relative humidity. In vacuum it is related to soft molecular bonding between the tip and the sample. This is also true in a liquid medium, although the adhesion force is usually lower than in vacuum because Van der Waals forces and other molecular bonding are usually softer when they act through water molecules and no capillary bridge is present.

The concept behind the force vs. distance curve can be generalized to the measurement of any other signal S as a function of the tip-sample distance, $S(z)$, e.g. oscillating amplitude, frequency shift or quality factor of the system. These experiments are usually called **spectroscopy** measurements with AFM.

1.5.2 3D-modes and *interaction images*

The so-called 3D-mode is a technique that expands the concept of spectroscopy measurements $S(d)$ to any other signal and parameter. It consists on registering any signal from AFM as a function of two parameters, $S(x, y)$, where S can be the same signals as in section 1.5.1 and x and y any parameter that can be controlled within AFM, e.g., tip-sample distance, biased voltage applied between tip and sample, oscillating amplitude, frequency shift or xy-position.

Interaction images[31] are a particular case of these 3D-modes where the signal that is registered is usually the normal force or the frequency shift and the parameters that are varied are the tip-sample distance as the slow scan and the biased voltage applied between tip and sample as the fast scan, $F_N(U_{bias}, z)$ or $\Delta\nu(U_{bias}, z)$ as shown in figure 1.3. This technique is fundamental to understand the work in this thesis since it underlies the basis to properly discriminate between different contribution to the total tip-sample interaction.

Chapter 2

Applied experimental and theoretical methods

2.1 Electrostatic properties at the nanoscale

2.1.1 The simplest model: tip-sample system as a parallel-plate capacitor

For applying this technique we assume that the tip-sample system in AFM behaves as a capacitor. A capacitor is an electrical system formed by two separated conductors. If we put a charge $+Q$ on one of them and $-Q$ on the other, since the the voltage is constant over a conductor, we can speak about a potential difference between the two conductors,

$$V = V_{+} - V_{-} = -\int \mathbf{E} \cdot d\mathbf{l}. \tag{2.1}$$

Since $\mathbf{E}$ is proportional to Q because of the Coulomb's law, so also is V and the constant of proportionality between Q and V is called the **capacitance** of the system and defined as

$$C \equiv \frac{Q}{V}. \tag{2.2}$$

Capacitance is a geometrical quantity and it defines how much charge the system can store by applied voltage. C is measured in farads, which is defined as coulomb per volt ($F = C/V$).

The simplest model of capacitor is the so-called parallel-plate capacitor represented in figure 2.1. This capacitor consists of two metal surfaces of area A separated by a gap of thickness d. It is assumed that the gap d is much smaller than the dimensions of the plates. Charge Q distributes uniformly over the plates with a surface charge density of $\sigma = Q/A$. For this system, the electric field between the plates has a constant magnitude of σ/ϵ_0 and is perpendicular to the plates and directed from the positive charged plate to the negative one. Therefor,

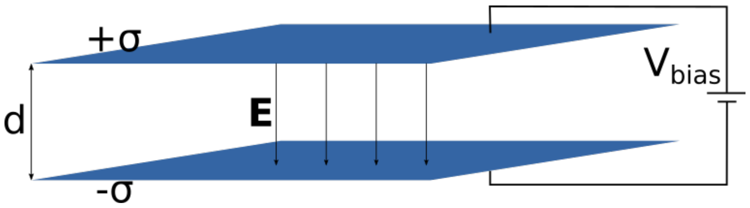

Figure 2.1: Diagram of parallel-place capacitor

the potential difference between the plates is

$$V = Ed = \frac{Q}{A\epsilon_0}d, \tag{2.3}$$

and the capacitance of the system,

$$C = \frac{Q}{V} = \frac{A\epsilon_0}{d}. \tag{2.4}$$

The electrostatic energy of a continuous charge distribution can be expressed in terms of the electric field as

$$W_{estat} = \frac{\epsilon_0}{2}\int E^2 dv, \tag{2.5}$$

where ϵ_0 is the vacuum permittivity and $\mathbf{E}$ is the electric field created by the charge distribution. The energy stored in the parallel-plate capacitor can be easily calculated from this expression and turns out to be

$$W_{estat} = \frac{\epsilon_0}{2}\left(\frac{Q}{A\epsilon_0}\right)^2 A\,d = \frac{1}{2}QV = \frac{1}{2}CV^2. \tag{2.6}$$

When we apply a known potential difference $V = V_{bias}$ between the plates, then

$$W_{estat} = \frac{1}{2}CV_{bias}^2. \tag{2.7}$$

In a more general case in which the plates are made of different materials, the potential difference has additional contribution due to the classic contact potential (V_{CP}) associated to the work function difference ($\Delta\phi$) between the two materials, $V = V_{CP} = \Delta\phi/e$, where e is the electron charge, and so

$$V = V_{bias} - V_{CP} \tag{2.8}$$

2.1.2 Work functions and contact potential

In solid-state physics, the work functions is the minimum thermodynamic work needed to transfer and electron from the Fermi level (E_{Fermi}) of a solid to a point in the vacuum outside the solid surface. The work function is not a characteristic of a bulk material, it is a property of the surface of the material and it depends strongly on the crystal face as well as on any oxide layer and any other atoms or molecules adsorbed on the surface. It even depends on the state of the adsorption of the atoms and molecules. So the work function changes on a polycrystalline surface from one grain to another and different work functions can be measured on the same surface.

The contact potential (V_{CP}) arises when two surfaces, one opposite the other, with different work functions (ϕ_1 and ϕ_2) come into electrical contact. Some electrons travel from the surface with lower work function (ϕ_2) to the surface with the higher work function (ϕ_1). Therefore, the electron-yielding surface is positively charged, while the surface that receives electrons is positively charged. This creates an electric field that makes it hard for the electrons to keep flowing. Equilibrium is achieved when electrochemical potentials are equalized, this is when $eV_{CP} = \phi_1 - \phi_2$.

If we apply this to the parallel-plate capacitor we studied before, we have that if we chose V_{bias} to be equal to the contact potential difference V_{CP}, then the electric field is zero, there is no potential difference between the plates and the capacitor is discharged. In such a case $V_{CP} = V_{bias}$ and if we know the value of the work function of one of the materials (let us suppose we know ϕ_2), then the other one can be calculated easily

$$\phi_1 = eV_{bias} - \phi_2. \tag{2.9}$$

2.1.3 Tip-sample system

I said before that we where using the parallel-plate capacitor as a simple model to understand how the tip-sample system behaves when we apply a potential difference between them. In AFM, the tip-sample system can be modeled as a capacitor with a complex geometry, where $\mathbf{E}$ is not uniform and depends on the tip-sample distance (z). However, the electrostatic energy of the capacitor formed by the metallic tip and sample can still be expressed as

$$W_{elec} = -\frac{1}{2}C(z,\zeta_i)V^2, \tag{2.10}$$

where $V = V_{bias} - V_{CP}$ is the potential difference between the tip and the sample and $C(z,\zeta_i)$ is the capacitance of the tip-sample system as a capacitor, which now depends on the tip-sample distance (z) and the geometry of the system (ζ_i), where parameters like the tip radius (R), the angel of the cone (θ) and the height of the tip (H)—as seen in figure **??**—are included.

For metallic substrates and tips the capacitance of the tip-sample system has been widely modelated applying different geometries for the tip. Analytical expressions have been obtained for the simplest model of an spherical tip. However, due to the long range of electrostatic interaction, this simplified model is not enough in many situations and other models are needed where more realistic geometries for the tip are applied. With this in mind, approximate analytical expressions have been obtained that include the contributions of the cone and the cantilever.

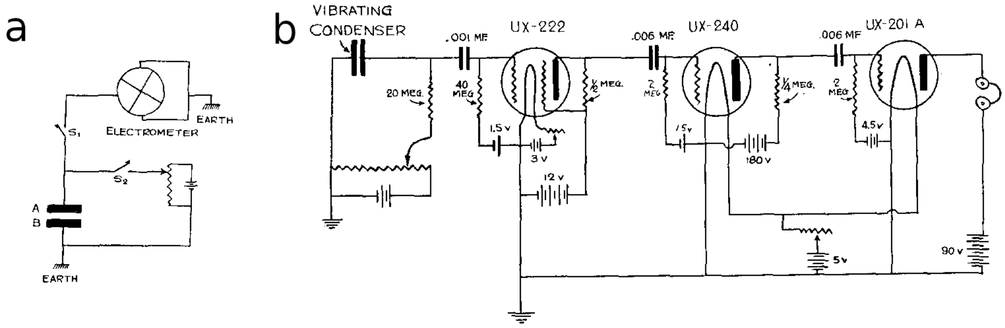

Figure 2.2: a) Lord Kelvin's method to measure contact potential differences in metallic samples and b) Zisman's improvement to the original setup introducing an acustic system. Both images are extracted from Ziman's paper[33].

Also for dielectric thin films and certain tip-sample distances, approximate analytical expressions have been obtained generalizing the expression for the metallic model. For thick dielectric samples, the capacitance of an spheric metallic tip close to the thick dielectric layer has been studied numericaly. In a rigorous way, the expression 2.10 is valid only for conductive or pure dielectric tips and samples, where V_{CP} does not depend on the tip-sample distance z nor the applied voltage V_{bias}. In the case where one of the materials is a semiconductor, the work function ϕ of the semiconductor can be modified when approximated to a metallic surface due to the induced band bending. In this case, the expression 2.10 can be extended to

$$W_{elec} = -\frac{1}{2}C(z, \zeta_i, V_{bias})(V_{bias} - VCP(z, V_{bias}))^2. \qquad (2.11)$$

2.1.4 Conventional Kelvin method

Lord Kelvin developed a technique to measure contact potencial differences[32] back in 1898. As explained by Zisman [33] back in 1932, Kelvin's method was based in the fact that when to dissimilar metal plates are places in contact they become charged with electricity of opposite polarity and a potencial difference (V_{CP}) can be measured between them that is independent of the relative position of the plates. Kelvin's original experiment—shown in figure 2.2—consisted on a variable parallel-plate capacitor. One of the plates was the sample while the other one was a plate made of a known metal that was moved forward and backward by hand. The capacitance of this moving capacitor varied within the movement of the plates and as a result a current was induced on the circuit that connected both plates. If the applied potential difference V_{DC} was equal in magnitude but opposite in direction to V_{CP}, then the charge would neutralize and the electrometer needle would not move. In that particular case $V_{CP} = -V_{DC}$.

Kelvin's method was quite slow in performance and the manipulation of the sensitive electrometer was not easy at all. For those reasons, Zisman improved the method by replacing the electrometer by an acustic system and using a vibrating capacitor so that an audio-frequency signal would be heard until the applied potential difference would balance the V_{CP}. With this new setup—that is shown in figure 2.2— contact potential could be measured with sensitiviy to $1\,mV$ in a few seconds of operation.

2.1.5 KPFM

The AFM was first used for measuring electric potential differences by Weaver and Abraham [34] and some months later, with a slightly different setup that allowed to monitor topography and contact potential difference (CPD) at the same time, Nonnenmacher et al. [35] used it to measure contact potential differences and called that technique Kelvin probe force microscopy (KPFM) for the first time. With this technique they were able to measure contact potential differences between different metallic materials with a high resolution for both the contact potential difference (better than $0.1\ mV$) and the lateral dimension (better than $50\ nm$).

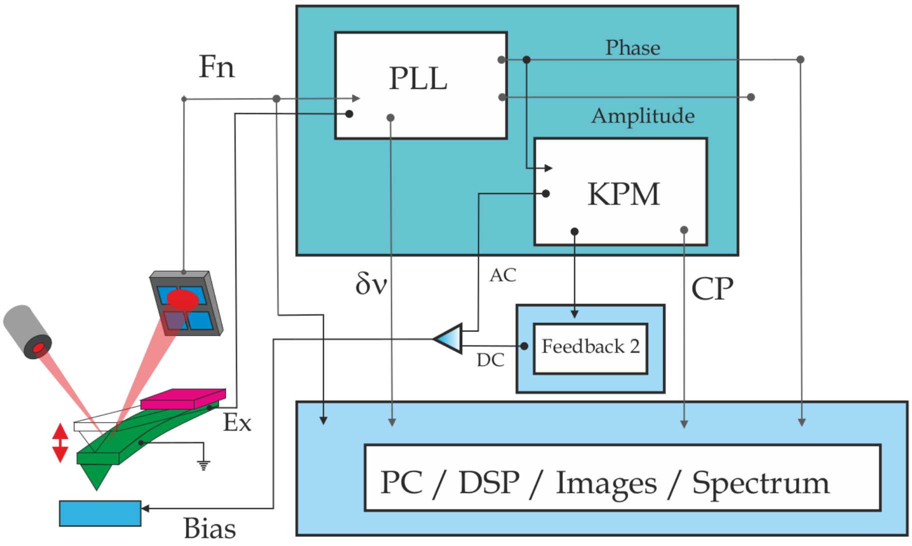

Figure 2.3: Usual experimental scheme for KPFM

2.2 Driven harmonic oscillators and its representation in the phase space

Considering the simplest version of the problem,the strap movement can be modeled by means of a damped and forced harmonic oscillator. Starting from the damped harmonic oscillator model, the differential equation that governs this problem is given by

$$m\ddot{x}(t) + \gamma\dot{x}(t) + cx(t) = F(t), \tag{2.12}$$

where m is the effective mass of the strap, γ is the damping constant, c is the elastic constant of the system and $F(t)$ is the externally applied driven force. With definitions: $\omega_0 = (c/m)^{1/2}$, $Q = c/(\omega_0\gamma) = m\omega_0/\gamma$, and assuming an harmonic driven force $F(t) = ma_0\omega_0^2 \cos(\omega t)$, where a_0 is a displacement determined by the driven force ($a_0 = F(0)/c$), this equation can be transformed into

$$\ddot{x}(t) + (\omega_0/Q)\dot{x}(t) + \omega_0^2 x(t) = a_0\omega_0^2 \cos(\omega t). \tag{2.13}$$

Using complex notation, this equation can be solved algebraically using the classical ansatz[1] $x(t) = \mathrm{Re}(\alpha(\omega)e^{i\omega t})$ for the steady state:

$$\begin{aligned}\mathrm{Re}(-\omega^2\alpha(\omega)e^{i\omega t}) + (\omega_0/Q)\mathrm{Re}(i\alpha(\omega)e^{i\omega t}) + ...\\ ... + \omega_0^2\mathrm{Re}(\alpha(\omega)e^{i\omega t}) = \mathrm{Re}(a_0\omega_0^2 e^{i\omega t}),\end{aligned} \tag{2.14}$$

from where the complex amplitude is determined

$$\alpha(\omega) = \frac{a_0}{1 - (\omega/\omega_0)^2 + i(\omega/\omega_0)/Q}. \tag{2.15}$$

A complex gain can be defined from 2.2 as

$$G(\omega) = \frac{1}{1 - (\omega/\omega_0)^2 + i(\omega/\omega_0)/Q}, \tag{2.16}$$

so that $\alpha(\omega) = a_0 G(\omega)$. Combining the previous relations we conclude that the displacement $x(t)$ is given by

$$x(t) = x_h(t) + A(\omega)\cos(\omega t + \phi), \tag{2.17}$$

where $x_h(t) \propto e^{-t/(2Q)/\omega_0}$ is the homogeneous solution and $A(\omega) = |a(\omega)|$. When $t \gg 2Q/\omega_0$, we have as a stationary solution

$$x(t) = A(\omega)\cos(\omega t + \phi), \tag{2.18}$$

where

$$\phi(\omega) = -\tan^{-1}\left(\frac{(\omega/\omega_0)/Q}{1 - (\omega/\omega_0)^2}\right) = -\pi/2 + -\tan^{-1}\left(\frac{(1 - \omega/\omega_0)^2}{1 - (\omega/\omega_0)/Q}\right) \tag{2.19}$$

represents the phase describing the delay between the excitation driven force and the response of the system, and

$$A(\omega) = |\alpha(\omega)| = \sqrt{X^2(\omega) + Y^2(\omega)} = \frac{a_0}{\sqrt{\left(1 - (\omega/\omega_0)^2\right)^2 + (\omega/(\omega_0 Q))^2}} \tag{2.20}$$

---

[1] An educated guess that is verified later by its results.

is the oscillating amplitude. Note that $A(\omega)$ is a function of ω that reaches a maximum value for a specific value of ω. By calculating the maximum of function $A(\omega)$, we find that this value is $\omega_R = (\omega_0 Q)/\sqrt{Q^2 - 1}$, which can be conveniently approximated (provided that $Q^2 2 \gg 1$) to $\omega_R \approx \omega_0$. For the following discussion, it is more convenient to write the complex amplitude $\alpha(\omega)$ in Cartesian coordinates:

$$X(\omega) = a_0 \frac{1 - (\omega/\omega_0)^2}{(1 - (\omega/\omega_0)^2)^2 + ((\omega/\omega_0)/Q)^2} \tag{2.21}$$

$$Y(\omega) = a_0 \frac{(\omega/\omega_0)/Q}{(1 - (\omega/\omega_0)^2)^2 + ((\omega/\omega_0)/Q)^2} \tag{2.22}$$

where $X(\omega)$ and $Y(\omega)$ are the phase and out-of-phase components of the oscillation. For complex amplitude one has then that $\alpha(\omega) = X(\omega) - iY(\omega)$ and the response to the excitation $a_0\omega_0^2 \cos(\omega t)$ is $a(t) = X(\omega)cos(\omega t) + Y(\omega)sin(\omega t) = A(\omega)cos(\omega t + \phi(\omega))$, where $\phi(\omega)$ is the phase between the excitation force and the response. At the natural frequency ω_0 the phase is $-\pi/2$, the (complex) amplitude of oscillation is $\alpha(\omega_0) = -iY(\omega_0) = -ia_0 Q$ and the component in-phase $X(\omega/\omega_0)$ is cancelled.

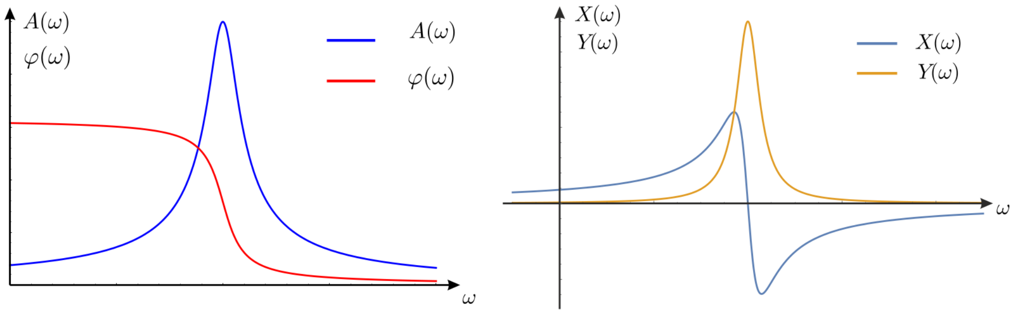

Figure 2.4: To the left the form that the curves $A(\omega)$ and $\phi(\omega)$ take can be seen when they are represented, while to the right the representation of $X(\omega)$ and $Y(\omega)$ is shown.

In the phase space the representation of the components $X(\omega)$ and $Y(\omega)$ allows a view of the interaction between tip and sample, as well as of the different dynamic modes. In a sweep in frequency, the representation in the complex plane of these components is, in good approximation, a circumference. When both components are represented by a fixed frequency, the graph is, approximately, a point that we will call (X, Y). By varying the frequency ω, this point describes a two-dimensional curve $(X(\omega), Y(\omega))$. Depending on the dynamic mode used in an experiment, this point will present variations that can be seen directly on an oscilloscope and contain information on how the point-sample interaction behaves (see figure 2.6).

The described circumference can be visualized directly from the graphical representation of the complex amplitude $\alpha(\omega)$ in the complex plane determined by

$(X(\omega), Y(\omega))$, as it can can be seen in figure 2.5. The theoretical equations that describe our system and the results are intuitively linked through these circumferences.

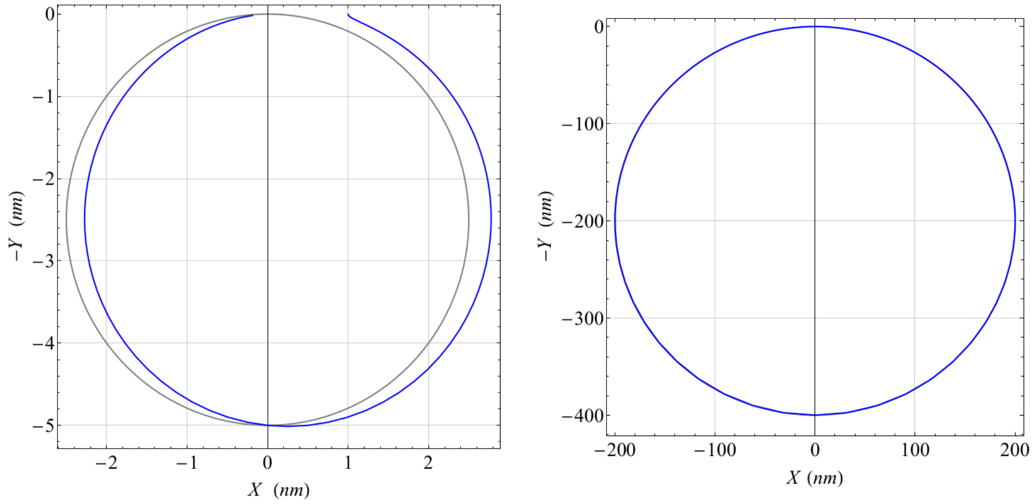

Figure 2.5: For both representations it has been used $a_0 = 1\,nm$, for the one on the left $Q = 5$ and for the right $Q = 400$. The gray curve in the first graph corresponds to a circle centered on $Q/2$ and of the same radius a_0. In the second graph, the circle is completely covered by the $\alpha(\omega)$ curve. Note that the minimum value is approximately $a_0 Q$.

In figure 2.5 it can be seen that the curve $(X(\omega), Y(\omega))$ corresponds approximately to a circumference, and that this correspondence becomes more accurate the grater the Q is. The resemblance to the circumference is surprising because the parametrization $\{X(\omega), Y(\omega)\}$ does not resemble the canonical one $\{cos(t), sin(t)\}$ for a circumference. These curves $(X(\omega), Y(\omega))$ will be named in this thesis as *circles*.

In resonance, conservative and non-conservative interactions will give rise to orthogonal variations in the phase space (see figure 2.6). In the case of conservative interactions, the gradient of the force results in a shift in the resonance frequency (as in the case for interactions of type $V_{sup} = c_f z^2$). For non-conservative interactions, dissipative interactions, this will be reflected in a reduction in the quality factor and therefore in a smaller amplitude (in the graph, in a smaller $Y(\omega)$ component): $\alpha(\omega_0) = i\omega_0 Q$. These variations due to the dissipative interactions are not reflected in the equations obtained for $X(\omega)$ and $Y(\omega)$, but they are already studied in literature[36, 37].

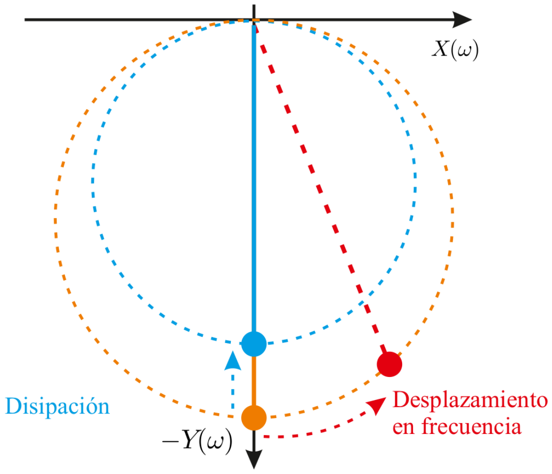

Figure 2.6: Representation of the amplitude $\alpha(\omega) = X(\omega) - iY(\omega)$ in the complex plane. The coarse point represents what is observed in the oscilloscope in an experiment. The different colors show the variations it suffers as a function of the present interaction. The dotted trajectories represent the path that the coarse point would follow if a sweep in frequency is made.

2.3 True non-contact mode

Among the community who operates the AFM in air, it is common to classify modes of measurement into attractive or repulsive regimes or into contact and non-contact modes. One of the most solid conclusions revealed by this work is that those of us who work with AFM in air have to take a further step in our quest to find quantitative and reproducible results as it will be show in the following chapters.

For this purpose, it is essential to have a well-defined interaction between the tip and the sample. Non-conservative capillary forces created by the capillary bridges that form and break between the tip and the sample when the distance is small enough introduce non-linearity that makes it difficult to collect data and analyze them with well-defined models.

For this reason we introduce what we call the **true non-contact mode** (to differentiate it from the traditional non-contact mode) as a measurement mode in AFM, generally operated in frequency modulation, characterized by small amplitudes of oscillation at a sufficient distance from the sample to prevent the formation of liquid necks between the tip and the sample. Only in this case, the only contributions to the total interaction between tip and sample are the electrostatic and van der waals interactions.

2.4 RCA cleaning standard

For cleaning of the cantilevers the RCA process has been used[38, 39]. In our experiments the two steps of the process are implemented as follows: The first step, Standard Clean-1 is performed with a solution composed of $5:1:1$ parts by volume of Milli-Q Water, NH_4OH (ammonium hydroxide, 29%) and H_2O_2 (hydrogen peroxide, 30%). When utilized as sample, the chips with the cantilevers are sonicated for about a minute in this solution, which removes organic residues. Before the next step the samples are rinsed with Milli-Q Water. The second step (Standard Clean -2) is performed with a solution composed of $5:1:1$ parts by volume of Milli-Q Water, H_2O_2 (hydrogen peroxide, 30%), and HCl (hydrochloric acid, 37%). Again, the cantilevers are sonicated for about a minute in this solution and then rinsed with plenty of Milli-Q Water. This second step removes metallic (ionic) contaminants that may have been deposited in the Standard Clean-1 cleaning step. In addition, for silicon surfaces this second step forms a thin passivating layer. Finally, the surface of the samples is dried by blowing with N_2 for about 1 minute.

This method is used in this thesis to clean almost every metallic or semiconductor sample unless any other method is described. Sometimes we combine this chemical method with other physical methods such as annealing or flaming.

2.5 Tip modelling

We start from a generic intermolecular potential of the form

$$w(r) = -\frac{C}{r^n}, \tag{2.23}$$

and a flat sample which is represented by a semi-infinite body defined by

$$S := \{(x, y, z) \mid z \leq 0\}, \tag{2.24}$$

while the tip is represented by the following solid of revolution

$$T(d) := \{(x, y, z) \mid z \geq c\rho^\mu + d,\ where\ \rho = \sqrt{x^2 + y^2}\} \tag{2.25}$$

which correspond with a cone for $\mu = 1$ and with a paraboloid of revolution for $\mu = 2$. d is the distance between the tip and the sample, as seen in figure 2.7, where the frame of reference is defined. To work out the total interaction energy between the tip and the sample we have to proceed to integrate the interaction for every pair of molecules in the tip and then sample as follows

$$\begin{aligned} W(d) &= \int\limits_{T(d)} n_T \, \mathrm{d}V_T \int\limits_{P} n_S \, \mathrm{d}V_S \frac{-C}{|\mathbf{r}_P - \mathbf{r}_{T(d)}|^\nu} \\ &= -C \int\limits_{T(d)} n_T \, \mathrm{d}V_T \int\limits_{P} n_S \, \mathrm{d}V_S \left((x_P - x_T)^2 + (y_P - y_T)^2 + (z_P - z_T)^2\right)^{-\nu/2}. \end{aligned} \tag{2.26}$$

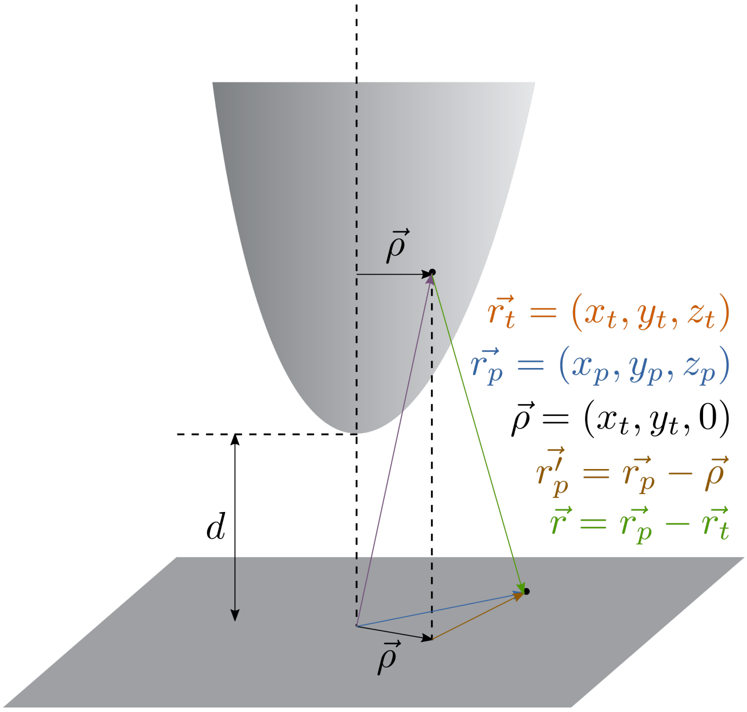

Figure 2.7: Frame of reference for the integration between each infinitesimal element of the tip with each infinitesimal element of the surface.

At this point we perform the following variable substitution $\mathbf{r}_P \to \mathbf{r}'_P = \mathbf{r}_P - \rho$, *where* $\rho = (x_T, y_T, 0)$. Within this new variable we have that $\mathrm{d}V_S = \mathrm{d}V'_P = 2\pi\rho\,\mathrm{d}\rho\,\mathrm{d}z'_P$, and hence, the expression goes like this

$$W(d) = -2\pi C n_S \int\limits_{T(d)} n_T \mathrm{d}V_T \int\limits_{-\infty}^{0} \mathrm{d}z'_P \int\limits_{0}^{\infty} \rho \mathrm{d}\rho \left(\rho^2 + (z'_P - z_S)^2\right)^{\nu/2}, \tag{2.27}$$

where we can now integrate for the plane and we get

$$\begin{aligned} W(d) &= \frac{2\pi C n_S}{\nu - 2} \int\limits_{T(d)} n_T \mathrm{d}V_T \int\limits_{0}^{\infty} \mathrm{d}z'_P \frac{1}{(z'_P - z_T)^{\nu-2}} \\ &= \frac{2\pi C n_S n_T}{(\nu-2)(\nu-3)} \int\limits_{T(d)} \mathrm{d}V_T \frac{1}{z_S^{\nu-3}}, \end{aligned} \tag{2.28}$$

which can be integrated in the volume of the tip using cylindrical coordinate system taking advantage of the symmetry of revolution of the tip. In the cylindical system,

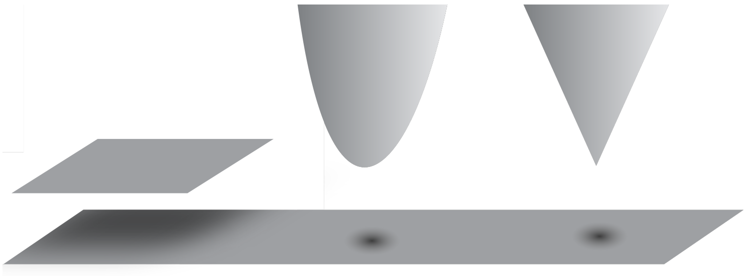

Figure 2.8: The interaction between the tip and the sample is calculated for three different models: two infinite planes, a parabolic tip and a plane and a conic tip and a plane.

where the angle has already been intregrated, the integral is like this

$$\begin{aligned} W(d) &= -\frac{(2\pi)^2 n_T n_S C}{(\nu-2)(\nu-3)} \int\limits_0^\infty \rho \mathrm{d}\rho \int\limits_{z=c\rho+d}^\infty \mathrm{d}z \frac{1}{z^{\nu-3}} \\ &= \frac{(2\pi)^2 n_T n_S C}{(\nu-2)(\nu-3)(\nu-4)} \int\limits_0^\infty \rho \mathrm{d}\rho \frac{1}{(c\rho^\mu + d)^{\nu-4}}, \end{aligned} \tag{2.29}$$

where the final solution depends on the particular value of μ (figure 2.8) that describes the geometry of the tip as a cone ($\mu = 1$) or as a paraboloid of revolution ($\mu = 2$). Integration on equation 2.29 can be continued to find the analytical solution taking also into account that for the cone-case $c = 1/tan(\alpha/2)$,

2.5.1 The tip as a cone

As it is mentioned before in the definition of the tip, expression 2.25, when $\mu = 1$ the tip is described as a cone. For this geometry the previous equation looks like this

$$\begin{aligned} &V_{cone}(d) \\ &= \frac{(2\pi)^2 n_T n_S C}{(\nu-2)(\nu-3)(\nu-4)} \frac{1}{c^2} \left[\frac{1}{\nu-5} \frac{d}{(c\rho+d)^{\nu-5}} - \frac{1}{\nu-6} \frac{1}{(c\rho+d)^{\nu-6}} \right]_0^\infty \\ &= -\frac{(2\pi)^2 n_T n_S C \; tan(\alpha/2)^2}{(\nu-2)(\nu-3)(\nu-4)(\nu-5)(\nu-6)} \frac{1}{d^{\nu-6}} \\ &= \frac{(\nu-7)!}{(\nu-2)!} \frac{(2\pi)^2 n_T n_S C \; tan(\alpha/2)^2}{d^{\nu-6}} \end{aligned} \tag{2.30}$$

Therefore, the acting force between both surfaces can be expressed as

$$F_{cone}(d) = \frac{(\nu-6)!}{(\nu-2)!} \frac{(2\pi)^2 n_T n_S C \; tan(\alpha/2)^2}{d^{\nu-5}}. \tag{2.31}$$

2.5.2 The tip as a paraboloid of revolution

On the other hand, particularising the other case study, that of a parabola where $\mu = 2$ and $R = 1/(2c)$,

$$\begin{aligned} &V_{parabola}(d) \\ &= \frac{(2\pi)^2 n_T n_S C}{(\nu-2)(\nu-3)(\nu-4)(\nu-5)} \frac{1}{2c} \left[(c\rho^{\mu} + d)^{-(\nu-5)} \right]_0^{\infty} \\ &= \frac{(2\pi)^2 n_T n_S C R}{(\nu-2)(\nu-3)(\nu-4)(\nu-5)} \frac{1}{d^{\nu-6}} \end{aligned} \tag{2.32}$$

Therefore, the acting force between both surfaces can be expressed as

$$F_{parabola}(d) = \frac{(\nu-5)!}{(\nu-2)!} \frac{(2\pi)^2 n_T n_S C R}{d^{\nu-4}}. \tag{2.33}$$

2.5.3 Plane-plane interaction

For the case in which two plane interacts with each other we can calculate the energy of that interaction per unit area, which is

$$\begin{aligned} &V_{plane}(d) \\ &= \frac{(2\pi)^2 n_T n_S C}{(\nu-2)(\nu-3)} \int_d^{\infty} \mathrm{d}\frac{1}{z^{\nu-3}} \left(2\pi \lim_{\rho\to\infty} \int_0^{\rho} \rho\rho \right) = \frac{(2\pi)^2 n_T n_S}{(\nu-2)(\nu-3)(\nu-4)} \frac{C}{d^{\mu-4}} \lim_{\rho\to\infty} (\pi\rho^2), \end{aligned} \tag{2.34}$$

from where the energy per unit area can be defined as

$$w(d) := \frac{\Delta V(d)}{\Delta A} = \frac{(\nu-5)!}{(\nu-2)!} \frac{2\pi n_T n_S C}{d^{\nu-4}}. \tag{2.35}$$

Conclusions

For a generic intermolecular potential such as the one described in equation 2.23 expressions have been found for the interaction force between the tip and the sample when the tip is parabolic and conical in shape.

In particular, it should be noted that for the parabolic tip, the interaction force and the energy between two semi-infinite bodies are related by the following expression

$$F_{parabola}(d) = 2\pi R w(d). \tag{2.36}$$

This expression is equal to that derive by Derjaguin[40, 41] as an approximation for the interaction between any two surfaces with local effective radius R so that $1/R = 1/R_1 + 1/R_2$. It is interesting and relevant to verify that this approximation found by Derjaguin becomes an exact relation for the case of the parabolic tip. This is very helpful in this thesis when we model the tip-sample interaction in chapter 4.

Chapter 3

Processing and analysis of interaction images

3.1 Introduction

An important part of the methodology discussed in chapter 4 is based on data processing. This processing is considered self important and definitely novel in the AFM community. Therefore it will be discussed in the present chapter.

There will be an obvious parallelism between this chapter and chapter 4 and references between them will be usual. As you should expect, data processing is adapted to how and in which format we acquire data but we also learn on how to better acquire data from its processing. It was therefore essential to develop the content of this subject on its own chapter because of its relevance.

3.2 Model

As pointed out on section 1.2, total force between tip and sample has many contributions. Their origin can be as different as electrostatic, van der Waals, capillary or elastic. It is one of AFM's objectives to develop techniques that allow to distinguish between those different contributions and analyze them separately. Only this way it is possible to understand the nature of the interaction between the tip and the sample and really extract the relevant information from them.

The most used AFM mode is the so-called AM-AFM and, when performed in air, it is characterized by relatively large oscillating amplitudes that result in an intermittent contact between the tip and the sample. As a result, in a typical AFM experiment under this conditions, the tip-sample interaction is comprised of the van de Waals and the electrostatic interactions in addition to a capillary interaction—due to the formation of capillary bridges between the tip and the sample—and an elastic interaction when the tip and the sample are in contacts,

$$F_{Total} = F_{VdW} + F_{Estat} + F_{Capillary} + F_{Elastic}. \tag{3.1}$$

The two latter contributions introduce an additional complication when modeling to model the tip-sample interaction that results in non-linear terms in the equations of motion of the oscillator that we want to prevent. That is why we try to avoid those contributions by making use of FM-AFM in our measurements. FM-AFM allows us to use smaller oscillating amplitudes as well as to keep the tip closer to the sample without forming capillary bridges. Nevertheless, doing so in air is tricky because of the layer of water that is always present on every surface when we work in air. It is there fundamental to have an appropriate software that is able to distinguish whether we are operating in a true non-contact mode or, on the contrary, capillary bridges are forming between the tip and the sample.

3.3 Acquiring experimental data

The spectroscopic measurements that we provide to the software to be analyzed are described in section 1.5.2 and consist of sitting the tip on a point of the surface and registering any signal within the AFM as a ramp bias voltage is applied for each tip-sample distance. This way we obtain an spectroscopic image of the measured signal and how it changes when we vary the tip-sample distance (vertical axis) and the applied voltage (horizontal axis).

From a point of view of the numerical analysis we have a file for each registered signal as the one described in the diagram of the figure 3.1 and that consists of two well-differentiated parts:

1. The header where all the parameters related to the AFM operation mode and to the measurement are stored.

2. The body of the file where the signal measurement itself is stored in a 16 bits ASCII format, where the value obtained for the signal is coded in terms of the position on the image rather than real physical magnitudes as position or voltage. Physical magnitudes can be inferred as well from the position and the data stored in the header.

3.3.1 Data acquired

Usually the signals we register are **normal force**, **amplitude**, **phase** and **frequency shift**, since they give us most of the information we need, although any other signal from SKPM, EAFM or any other AFM-based technique can be registered and analyzed within this method. As we will discuss later, each of the registered signals provides us with a variety of data related to the tip-sample system which will be essential for farther analysis.

In figure 3.2 we can see a selection of the different cases we can find during the experiments and how registered signals look like different for each case. Our software is programmed so it is smart enough to distinguish between them and apply a different algorithm depending on the particular case.

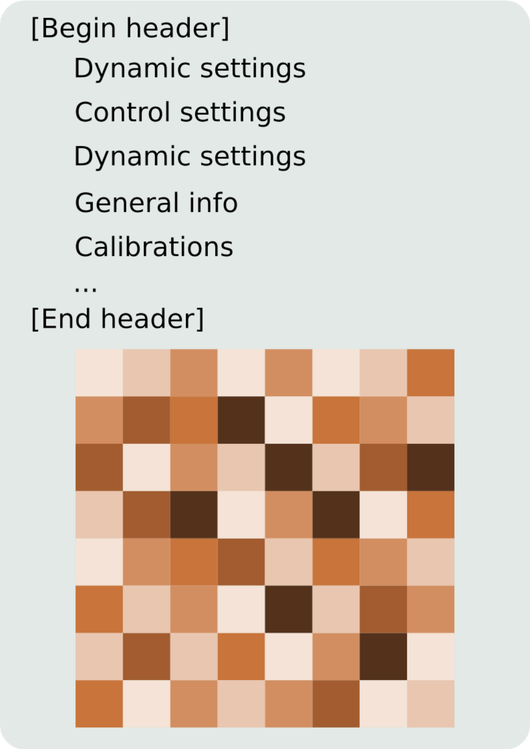

Figure 3.1: This is the structure that presents any file coming from WSxM, which is the program we use to control the AFM and saving the images.It present a header where all the parameters related to the AFM operation mode and to the measurement are stored and a body where the signal measurement itself is stored in a 16 bits ASCII format.

In the first row of figure 3.2 we can see the simplest case in which we start from a certain tip-sample distance that is reduced until tip and sample are very close but still far enough so that no capillary bridges are formed. Normal force, amplitude and phase keep constant in this case while the frequency shift changes as explained in section 1.5.2—it depends on the square of the voltage and and inverse power of the distance.

The second row in figure 3.2 corresponds to the case in which capillary bridges begin to form between the tip and the sample. There may even be intermittent contact between them at some point. This happens at the bottom of the images and two significant effects can be observed in this case. First, an important reduction of the amplitude (image f) is observed due to energy dissipation because of the capillary bridges formation. Secondly, in the phase signal (image g) the noise has increased significantly, again due to the formation of capillary bridges that introduce an additional phase between the driven signal and the response signal.

Finally, the third row shows the case in which the tip and the sample get into contact. Above contact, signals are equivalent to the previous cases and the same analysis can be applied. But after reaching contact the oscillation stops and all the

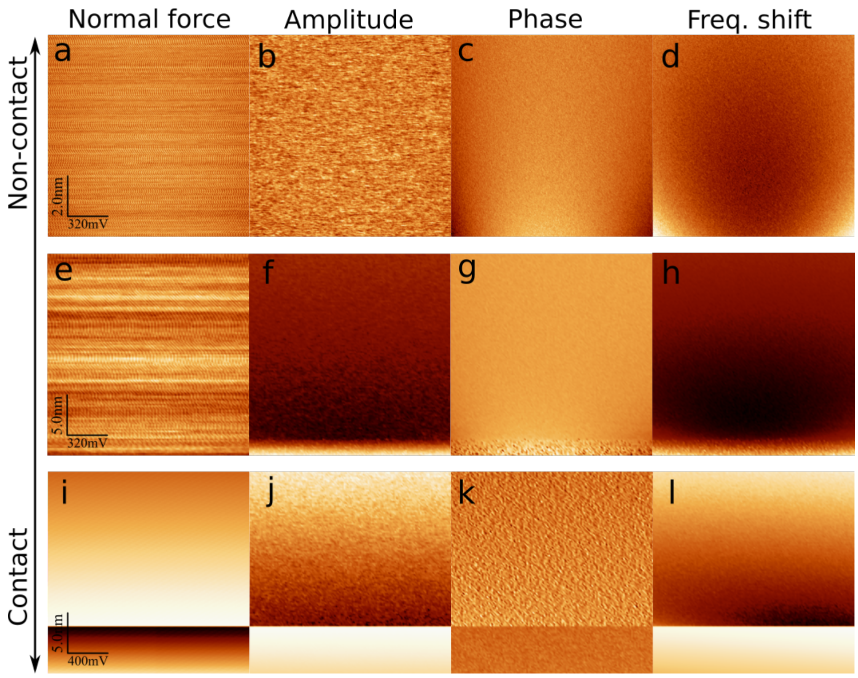

Figure 3.2: Interaction images of the normal force, amplitude, phase and frequency shift channels for three different cases. First row for a true non-contact regime. On the second row also a non-contact regime is showed where some capillary bridges start to form an break at the lower part. The images on the third row correspond to a classical contact regime.

dynamic signals goes to zero. Only the normal force—which is directly measured from the cantilever deflection—increases after contact as expected. Actually, every vertical line of the image i corresponds to a $F(z)$ curve. In figure 3.3 we can see the image i in figure 3.2 rotated $90°$ and the result of plotting a random vertical line in and represented as a function of tip-sample distance.

3.3.2 Additional data

2w and 1w when ESFM

3.4 Structure of the code

We divide the program into three different main blocks:

- The first one for the numerical processing and analysis of the measured data.
- The second block for converting into physical units and saving data.
- A third block for grouping similar experiments and defining the surface position.

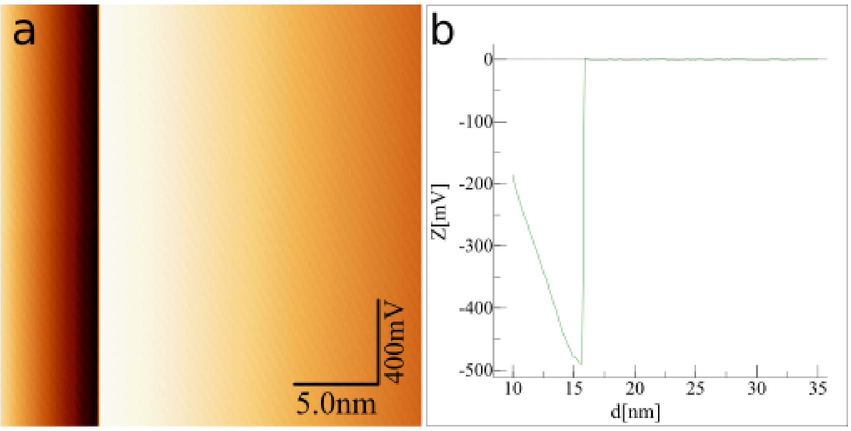

Figure 3.3: (a) Normal force interaction image rotated $90°$ to better understand how every line corresponds to a $F(z)$ curve, color scale corresponds to $500\ mV$, and (b) $F(z)$ obtained after plotting a line from the normal force interaction image.

3.4.1 First block: numerical analysis

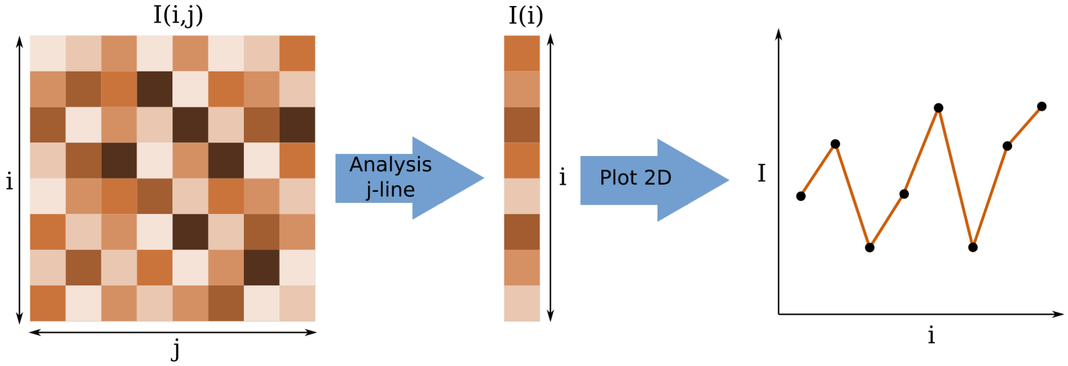

Figure 3.4: This is the diagram that graphically explains what is done in this block. Starting from an interaction image that depends on two parameters—tip-sample distance (vertical) and applied voltage (horizontal)—we extract spectroscopic curves as a function of the distance.

The first block of the program is dedicated to the numerical treatment of the interaction images, $I(i,j)$. Amplitude and phase interaction images do not depend on the applied voltage and it is relatively straightforward to reduce the data from the interaction images into spectroscopic curves that only depend on the tip-sample distance variable, $I(i)$. We also carry out the necessary numerical treatments to obtain the spectroscopic curves corresponding to the van der Waals and electrostatic interactions as well as the surface contact potential from the interaction images in frequency as well as in normal force. In figure 3.4 we can see a diagram that graphically explains what is done in this block.

At this point of the program it is convenient to keep working in terms of the points on the image better than already converting into physical units the vertical axis (distance) and the horizontal one (applied voltage). In this way, the adjustment to the parabola, among other processes, is greatly simplified and streamlined.

3.4.2 Second block: spectroscopic curves

In the second block, we assign a distance to each element of the curve according to its position in the list. This is possible because we know—from the header of the file—what the distance traveled Δd_{travel} is.

$$\begin{aligned} i \in \mathbb{N} : [1, N] \quad &\rightarrow \quad d(i) = \frac{i-1}{N-1} \Delta d_{travel}, \\ I(i) \quad &\rightarrow \quad I(d). \end{aligned} \tag{3.2}$$

It is important to point out that this distance is not absolute with respect to the position of the surface—which we do not know yet—, instead it is the last experimentally measured point.

3.4.3 Third block: grouping and selecting surface position

During the AFM measurement, we make several interaction images on the same point of the sample to be able to make a subsequent statistical treatment of the results. At this point of the code, this different measurements and results on the same spot of the sample are grouped and treated statistically to obtain a more precise result.

After the treatment and analysis of data, we are able to define in a more accurate way the position of the surface d_0 from the spectroscopy curves. This action is performed and represented graphically in this block.

3.5 Processing data

3.5.1 Amplitude

The amplitude of the vibrating cantilever does generally not change with the applied voltage but it does with the tip-sample distance. For that reason, from the amplitude image $A(d, U)$ we average every line to obtain a precise mean value for the amplitude at each tip-sample distance, $A(d)$. Also the standard deviation of the amplitude for each tip-sample $\delta A(d)$ distance is worked out as follows

$$A(i) = \langle A(i, j) \rangle_j \tag{3.3}$$

$$\delta A(i) = \sqrt{\frac{\sum_{j=1}^{N} A^2(i, j) - A^2(i)}{N-1}}, \tag{3.4}$$

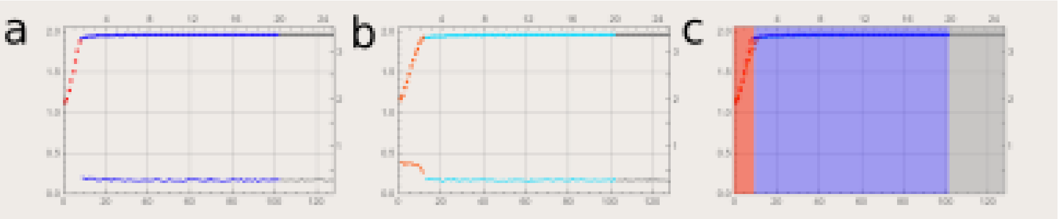

Figure 3.5: Pie de foto

where N is the number of pixels contained in each line of the image. In our experiments, usually $N = 128$ or 256.

From the analysis of this curve we obtain critical information for further processing. As explained before, it is crucial to stay in a true non-contact regime while we measure the interaction because only in that case the interaction corresponds to the sum of electrostatic and van der Waals interactions. This curve is used to find the point where capillary bridges start to form up because at that point additional forces start to act between the tip and the sample.

First we set the free amplitude oscillation far from the surface A_{free}—gray part of the plot—and then we compare with that value every point of the curve $A(i)$. As soon as we observe a significant reduction of the amplitude we assume that capillary bridges are forming up from that point on and, therefore, we remove those data from our analysis. You can see those points in red on the three graphics in figure 3.5, while point in blue don't present a significant difference with A_{free}.

3.5.2 Phase

We process the phase image similarly to how we process the amplitude image. We average every line to get a mean value for each tip-sample distance and the standard deviation for that mean value

$$Ph(i) = \langle Ph(i,j) \rangle_U \tag{3.5}$$

$$\delta Ph(i) = \sqrt{\frac{\sum_{j=1}^{N} Ph^2(i,j) - Ph^2(i)}{N-1}}. \tag{3.6}$$

We find that the phase signal is especially sensitive to the formation of capillary bridges between the tip and the sample. Noise in this signal increase considerably when capillary bridges start to form and break as we can clearly see in figure 3.2, image g, and figure 3.6.

3.5.3 Frequency shift

Using the amplitude and the phase signals the software is able to distinguish in which of the three cases we are. More important, it is able to distinguish which part of the data file correspond to the true non-contact regime (see figure 3.2)

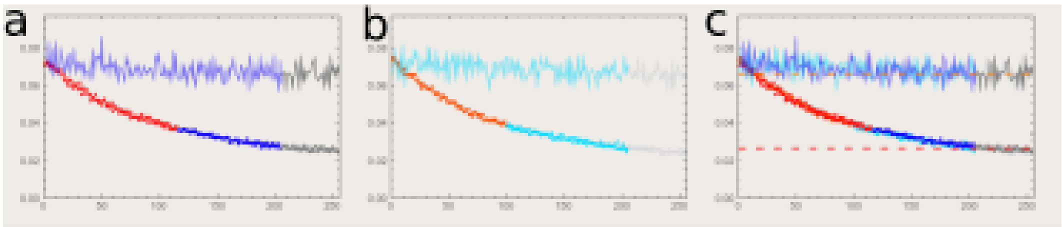

Figure 3.6: Pie de foto

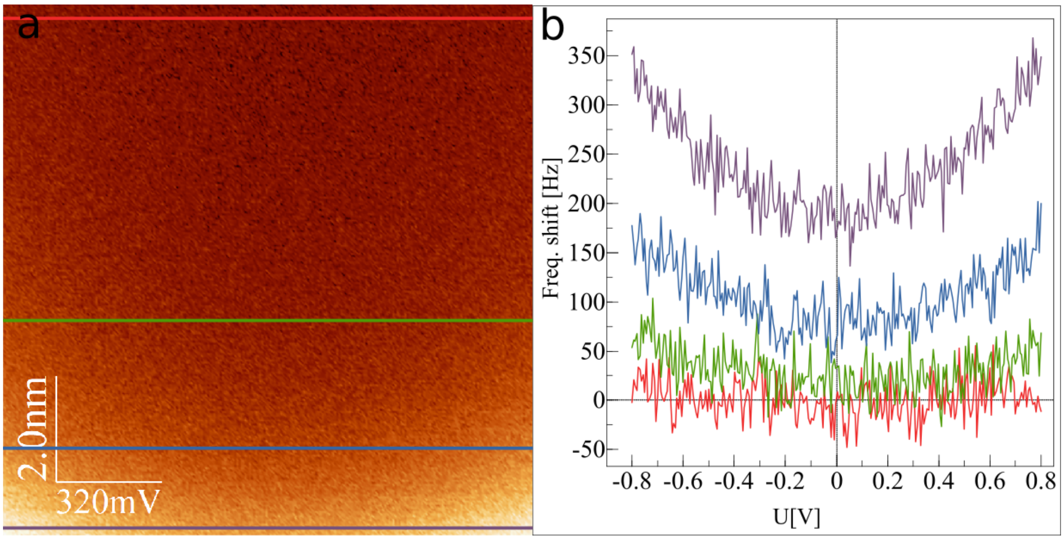

Figure 3.7: Pie de foto

and, therefore, can be used to reconstruct the electrostatic and the van der Waals interactions as well as the surface contact potential.

According to the theoretical model, at a fixed distance d, the frequency shift depends on the square of the applied voltage U. therefore, every line of the interaction image in frequency shift channel should be able to fit to a parabola as described in equation 4.14.

Here we can see a clear example of what we mentioned in section 3.4 about not converting into physical units for the first two blocks of the code corresponding to the numerical analysis of the measured data. As long as we keep the sampling points constant during data acquisition with the AFM—which we do in almost every experiment—the calculations for the fitting regarding to the applied voltage axis (x axis) only depend on the size of the images and are the same for all the images registered. Therefore those calculations can be done only once and used for every fitting.

For a $N \times N$ pixels interaction image—in our experiments, $N = 256$ usually—, every horizontal line has N points and, therefore, the coefficients corresponding to the x axis (applied voltage) are

$$\begin{aligned} \overline{x} &= \frac{\sum_{i=1}^{N} x_i}{N} = \frac{N+1}{2} \\ \overline{x^2} &= \frac{\sum_{i=1}^{N} x_i^2}{N} = \frac{(N+1)(2N+1)}{6} \end{aligned} \tag{3.7}$$

for all the fits. In this way, the fitting to the parabola is greatly accelerated. Fitting the experimental data to a parabola, for each (voltage) scan line three parameters are determined: the position of the minimum of each parabola, corresponding to the Contact Potential U_{CP}, the vertical offset of the parabola (measured interaction at the minimum of the parabola) corresponding to the Van der Waals interaction, and finally the curvature of each parabola, which is determined by the capacity, and thus by the strength of electrostatic interaction.

The curve obtained for $\Delta\nu_{VdW}(d)$ can be then fitted to the expression 4.9, while the curve obtained for $\Delta\nu_{estat}(d)$ can be to the expression 4.10. Here a problem arises, it is not easy to adjust experimental data to a curve that diverges at one point, d_0. The solution is to first estimate a value for the pole of those interactions by dividing the experimental data of both interactions and adjusting to the line defined in expresion 4.11. As it will be discussed later, from the fitting, the Hamaker constant and the value for d_0 (assuming it's the same for both interactions) is obtained.

On the other hand, the curve $U_{CP}(d)$ is also represented and fitted to a line. In case of conducting samples, the line should be flat. If the fit presents a slope, it means that there exist an electric field acting between the tip and the sample, and therefore, that implies that a surface charge density exists, $\sigma = \epsilon_0 E$.

3.5.4 Normal force

The analysis carried out on the interaction image in the normal force signal is similar to that of the frequency shift. Each of the scan lines in this signal, taken in true non-contact mode, can be adjusted to a parabola defined by the sum of the expresions 4.6 and 4.7. From the fitting of each of these lines three parameters are obtained for a given tip-sample distance: the contact potencial U_{CP}, the van der Waals interaction $F_{VdW}(d)$ and the electrostatic interaction $F_{estat}(d)$.

In adittion it is possible to analyse the curves $F(d)$ shows in figure 3.3 from where some parameters such us the distance to snap to contact d_{snap} or the adhesion force $F_{adhesion}$. These characteristics of this curves and its parameters are better described in the introduction chapter, in section 1.5.1.

Chapter 4

Determination of the Hamaker constant in metallic samples

4.1 Introduction

Interaction of dispersion forces of materials and their Hamaker constants are subjects of increasing interest. The use of the AFM for their study brings an opportunity for quantitative measurements as some previous studies have demonstrated[42].

The aim of this chapter is to develop an AFM-based technique for a quantitative study of the dispersion forces and electrostatic interactions that allow the calculation of the Hamaker constant in metals and semiconductors.

4.1.1 Van der Waals forces

There exist many interactions that act between atoms and molecules[41]. *Covalent* or *chemical forces* tightly bind atoms together to form molecules or crystals with well defined structures where the atoms lose their discrete nature and thus this interatomic bonds are called *covalent* or *chemical bonds*. Other forces arise from straightforward electrostatic interactions between charged or dipolar molecules, e.g., *ionic* or *Coulomb forces* that hold atomic or molecular ions together to form rigid lattices; the hydrogen bonding interaction that is specially relevant between water molecules interactions or dipole-dipole interaction between polar molecules[1]. However, there is one type of interaction which is always present between all atoms and molecules. They are known as *dispersion forces* and make up the most important contribution to the total Van der Waals force between atoms and molecules along with dipole-dipole (*orientation force*) and dipole-induced dipole interactions (*induction force*) as expressed in

$$W_{VdW}(r) = -[C_{ind} + C_{orient} + C_{disp}]/r^6 = -C_{VdW}/r^6. \tag{4.1}$$

---

[1] Shall I include table from The nature of van der waals forces, Israelachvili of molecular interactions?

Nevertheless, when we want to consider the interactions of macroscopic particles or surfaces, all the pair potentials between the molecules in each body have to be summed[2].

4.1.2 The Derjaguin approximation

The Derjaguin approximation[40] gives us a very interesting relation between interaction energies and interaction forces that results very useful interpreting experimental data. Specifically it gives the force between two spheres, with radii R_1 and R_2[3], in term of the energy per unit area of two flat surfaces at the same separation, d.

$$F(d) = 2\pi \frac{R_1 R_2}{R_1 + R_2} W(d) \tag{4.2}$$

The more surprising thing about tfhe Derjaguin approximation, and what it makes it so useful, is that it can be applied to any kind of force law if the range of the interaction and the separation are much smaller than the radii of the spheres.

4.1.3 Van der Waals interaction between particles and surfaces: the Hamaker constant.

This approximation can be used straightforward in our AFM experiment since we can approximate the tip-sample system in AFM as a sphere of radius R -the tip- separated by a distance d from a flat surface -the sample. This approximation is acceptable whenever it happens that R is larger than d.

Considering that the van der Waals interaction between two molecules is merely attractive and of the form $W(d) = -C_{VdW}/d^6$ as well as assuming additivity on the interaction, it is not difficult to sum all the pair potentials between the molecules in two flat planes to obtain the interaction energy between them per unit area[4]. This is

$$w_{VdW}(d) = -\frac{A}{12\pi d^2} \tag{4.3}$$

and thus, applying the Derjaguin approximation we obtain that the Van der Waals force between the tip and the sample is approximated by

$$F_{VdW}(d) = 2\pi R w_{VdW} = -\frac{AR}{6d^2}, \tag{4.4}$$

where A is the Hamaker constant[10] that models the van der Waals interaction for macroscopic bodies and it is dependent on the properties of the materials that the tip and the sample are made of.

---

[2] Escribir un párrafo sobre la importancia de las fuerzas de Van der Waals en muchos fenómenos físicos

[3] Let's note that a sphere close to a flat surface is a special case of two spheres, where the radius of one sphere is much larger than the radius of the other.

[4] Maybe here I should write something about how to get to the interaction energy between two flat planes from the molecular interaction and how Hamaker constant is defined...

4.1.4 State of the art

For gases, the London dispersion force coefficient C, and therefore the Hamaker constant A, is related to coefficient a in the van der Waals equation of state as follows

$$C = 3\sigma^3 a/2\pi N_0^2 \tag{4.5}$$

where $sigma$ is the diameter of the molecules of the gas for the hard spheres model and N_0 is the Avogadro constant. Experimental values for A can be obtained taking this into account for gases that can be described by the van der Waals equation of state.

Considering that the van der Waals interaction between two molecules is merely attractive and of the form $w(d) = -C_{VdW}/d^6$ as well as assuming additivity on the interaction, it is not difficult to sum all the pair potentials between the molecules in two bodies in order to obtain the interaction energy between them. This approximation is appropriate for rarefied gases where the additivity assumption is applicable.

The additivity assumption doesn't hold for condense matter since the effective polarizability of an atom changes when it is surrounded by other atoms. Therefore the Lifshitz theory[43, 44] of van der Waals forces must be introduced. It ignores the atomic structure of media. Instead, the bodies as treated as continuous media and the forces between them is derived in terms of their bulk properties as dielectric constants and refractive indices using quantum field theory. Very precise solutions can be computed from it[5].

4.1.5 Objectives

The goal of this work consists of looking for a method to chemically characterize samples within the Atomic Force Microscope (AFM). Several approximations can be taken into account for this purpose but we want to determine the Hamaker constant, A, of our samples as defined before since it is a material dependent constant.

4.2 Theoretical model

Let us start modeling the tip-sample system in AFM as a sphere with radii R separated a distance d from the sample surface where we are going to measure as seen in figure 4.1 and start from the expressions for the van der Waals and electrostatic forces for that precise geometry of the system. These are

$$F_{VdW}(d) = -\frac{A_{tip-sample}R_{tip}}{6(d-d_0)^2} \tag{4.6}$$

---

[5] Aquí se necesitan más referencias

Figure 4.1: The approximation to model the tip-sample system in AFM.

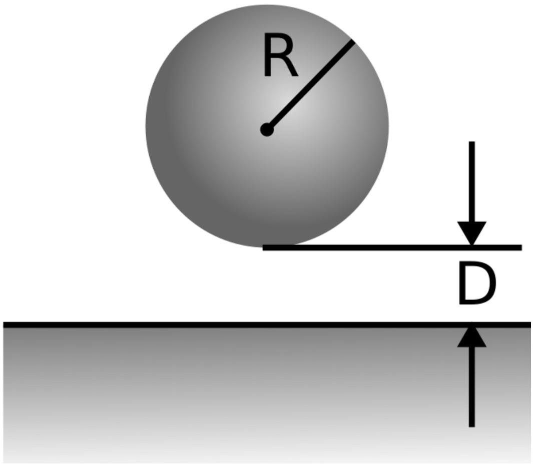

for the van der Waals force and

$$F_{estat}(d) = -\frac{\pi\epsilon_0 R_{tip}}{d-d_0}(U-U_{cpd})^2 \tag{4.7}$$

for the electrostatic force, where all the parameters are either well known or easy to control within the AFM except for the R_{tip}, d_0 and $A_{tip-sample}$. I point out that d_0 is introduced since we do not the precise position of the tip from the sample ant it will be another parameter to work out in our model.

In dynamic scanning force microscopy (DSFM), for small oscillating amplitudes, the frequency shift of the oscillating cantilever is closely related to the interaction forces between the tip and the sample as follows

$$\frac{\Delta\nu}{\nu} = \frac{1}{2c_{lever}}\frac{\partial F}{\partial d} = \tag{4.8}$$

so the contribution of both interactions to the frequency shift at the resonance frequency correspond to the expressions

$$\frac{\Delta\nu_{VdW}}{\nu_0} = \frac{1}{2c_{lever}}\frac{A_{tip-sample}R_{tip}}{3(d-d_0)^3} \tag{4.9}$$

$$\frac{\Delta\nu_{estat}}{\nu_0} = -\frac{1}{2c_{lever}}\frac{\pi\epsilon_0 R_{tip}}{(d-d_0)^2}(U-U_{cpd})^2 \tag{4.10}$$

We will see in the next section that we can use an spectroscopic technique in DSFM to separate both contributions from the total frequency shift signal as a funcion of the distance. AÑADIRE ALGO MÁS ANTES DE DIVIDIR LAS DOS SEÑALES

$$\frac{\Delta\nu_{estat}}{\Delta\nu_{VdW}}(d) = \frac{3\pi\epsilon_0}{A_{tip-sample}}(d-d_0) \tag{4.11}$$

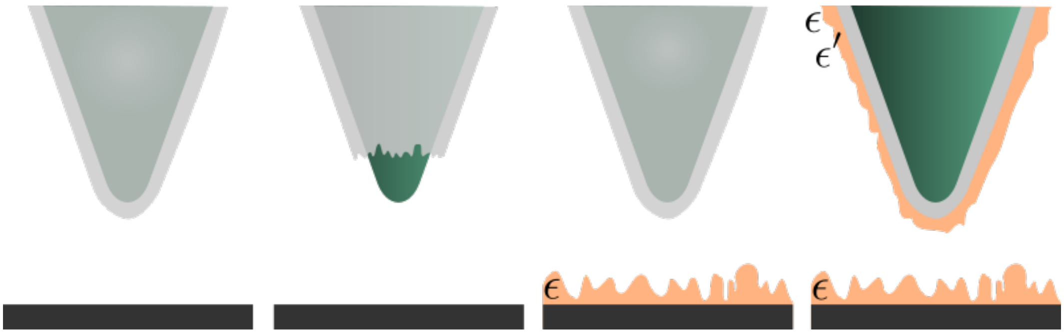

Figure 4.2: peeled tip

which describes a linear relation between the distance and the quotient of the two interactions that is not dependent on the geometry of the system anymore. Therefore the Hamaker constant $A_{tip-sample}$ and the real position of the sample d_0 could be calculated from a set of $\{(\Delta\nu_i, d_i)\}$ data.

We have made implicitly several assumptions in our model to get to this point that have to be confirmed experimentally. Some discussion is needed before carry on:

- The obvious one is that we are modeling the tip-sample system with a very simple model consisting on a sphere for the tip and a flat plane for the surface.

- We are also assuming that the effective geometry of the tip is the same for both interactions when it could happen that it is not. An example of a possible geometry of the tip can be seen in figure 4.2, where the tip has suffered some damage while operating and the conducting coating has been peeled off the tip apex.

- Finally we also assume that the effective position of the sample from the tip d_0 is the same for both interactions. This is very related to the previous one. If we have a look at the figure 4.2 again, it is easy to understand that the surface is farther from the conductive coating than from the remaining non-conducting tip apex.

4.3 Experimental validation and results

Some experiments have been performanced to experimentally validate the model previously exposed in section 4.2. The experiments consists of acquiring on-point frequency shift $\Delta\nu$ data on different conductive samples while the tip-sample distance d and the applied voltage U are varied.

4.3.1 Sample preparation

Samples consist on evaporated gold and platinum films and highly oriented pyrolytic graphite (HOPG). Tip as well as metallic samples are carefully cleaned using the RCA cleaning standard previously discussed in section 2.4. HOPG is exfoliated right before the experiment to have a fresh surface of it to measure. The cleaning process is extremely important, any residual organic contamination either on the tip or the sample would result on a lower effective Hamaker constant and therefore lower interaction.

4.3.2 Experiemental method

Before anything else, it is imperative to operate the AFM in the FM-AFM mode for several reasons. The first and most obvious reason is to prevent the tip from any damage or contamination coming from the surface. The tip is half of the tip-sample system. Any change on the sample surface is easily detected within the AFM itself during the experiment but we are completely blind to the tip so it is extremely important to be as careful as possible during the measurements to keep the tip safe. That means we need to precisely control the tip-sample distance at every time.

Moreover, as we previously discussed in section 1.2.1, tip-sample interaction is the result of adding any existing interaction between the tip and the sample. These interactions can be as many and as different as van der Waals, electrostatic, magnetic, capillary or elastic interactions.

$$F_{Total} = F_{VdW} + F_{Estat} + F_{Magnetic} + F_{Capillary} + F_{Elastic} + \dots \tag{4.12}$$

In our experimental model we consider exclusively van der Waals and electrostatic interaction, so we have to manage ourselves to avoid any other interaction beyond the mentioned ones. Magnetic interaction is not present in our system since neither the tip nor the sample are magnetic but any other interaction might be present since our experiments are performanced in air. AFM must be operated in a true non-contact mode to prevent the tip to touch the sample. This way we avoid both elastic forces and the formation of capillary bridges between the tip and the sample. And thus, we make sure that van der Waals and electrostatic are the only interactions contributing to the total force in the system.

$$F_{Total}\Big|_{FM-AFM} = F_{VdW} + F_{Estat} \tag{4.13}$$

The other important reason to perform these experiments in the FM-AFM mode is the need to stay as close to the surface as possible in order to increase the ratio between the signal and the error. Of course, always avoiding the formation of capillary bridges. Being close to the surface -some nanometers- means very small oscillation amplitude. In this situation frequency shift signal is much more

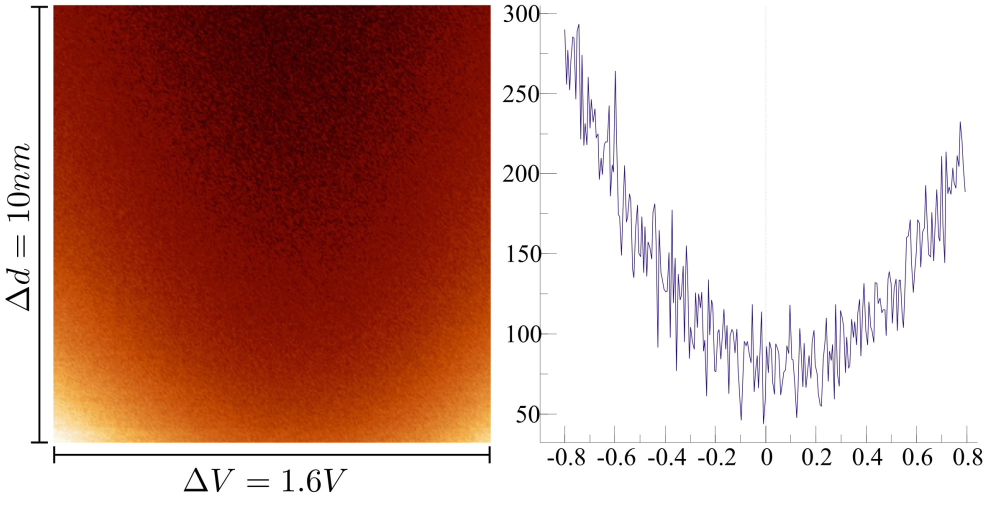

Figure 4.3: Frequency interaction image.

sensitive to small changes than the amplitude signal so it let us to stay closer to the surface with no tapping effect[45].

All these three reasons make imperative the use of the FM-AFM mode in our experiment.

4.3.3 Interaction images

Interaction images are well defined and explained in section 4.3.3 and in the literature[31], where I encourage the reader to head for deeper explanations and other applications.

A priori, only total interaction is measured and some technique to discriminate between each component, van der Waals and electrostatic in our case. For this purpose we use a technique that allows the precise and quantitative measurement of the tip-sample interaction. It is based on the measurement of tip-sample interaction not only as a function of tip-sample distance, but also as a function of tip-sample voltage. This is what we call *interaction images*. Only electrostatic interaction depends on the variation of the applied bias, so this will enable us to discriminate between both interactions. Using an appropriate data processing algorithm both interactions can be determined as a function of the tip-sample distance and thus the theoretical model exposed on section 4.2 can be applied.

On the left image in figure 4.3 we have a frequency interaction image as defined before. The horizontal axis represent the fast scanned variable, the bias U, while the vertical axis represent the slow scanned variable, the tip-sample distance d. At this point we recall that for a fixed distance d_{line} the change in the frequency shift due to the total tip-sample interaction is given by equation 4.8 and it is of the form

$$\frac{\Delta\nu}{\nu_0}(d,U)\bigg|_{d=d_{line}} = \alpha(d_{line}) + \gamma(d_{line})(U - \kappa(d_{line})^2)/2 \tag{4.14}$$

where the constant term $\alpha(d_{line})$ describes the van der Waals interaction (equation 4.9); $\gamma(d_{line})$, the curvature of the parabola induced by electrostatic interaction, describes the second derivative of the tip sample capacity and $\kappa(d_{line})$, the position of the minimum of the parabola, is the term associated with the local contact potential U_{cpd} (equation 4.10).

The quadratic dependence of tip-sample interaction on voltage is essentially the basis for the separation of van der Waals and electrostatic interactions[46, 47].

By measuring a family of curves $\Delta\nu/\nu_0(d_{line}, U)$ as a function not only of tip voltage U but also of tip-sample distance d, interaction images $\Delta\nu/\nu_0(d,U)$ are obtained; see images on figure 4.3. Each horizontal line $\Delta\nu/\nu_0(d_{line}, U)$ of the interaction image is then adjusted to the parabola defined by equation 4.14 to obtain the contribution of the van der Waals interaction, the contact potential and the tip-sample capacitance. A whole interaction image $\Delta\nu/\nu_0(d,U)$ results in three curves $\alpha(d)$, $\gamma(d)$ and $\kappa(d)$ characterizing the van der Waals interaction, the capacitance and the contact potential as a function of tip-sample distance as seen in figure 4.4[6]

4.3.4 Data processing and results

Data are processed as follows. As we have previously explained in section 4.3.3, from interaction images we obtain the curves that describe the van der Waals and the electrostatic interaction as a function of the tip-sample distance. Also $U_{CP}(d)$ curves are obtained. After that, the quotient between both interactions is worked out. A linear regression analysis on the resulting curve is applied. Comparing the results to the expression 4.4 we notice that the Hamaker constant A can be calculated from the slope of the linear regression while the tip-sample distance offset d_0 is calculated from the intercept.

Fitting results in effective averaging of data, since each data point can be considered an independent experiment. Also quality of the fit to a regression line is a direct check of validity of theoretical background (e.g. spherical tip and $d_0^{estat} = d_0^{VdW} = d_0$).

This method has been applied to metal and conducting samples and the Hamaker constant has been experimentally calculated. The resulting values for gold, platinum and HOPG are showed in figure 4.5.

---

[6] En la figura no aparece el CP como reza el párrafo; solamente VdW, electrostática y su cociente.

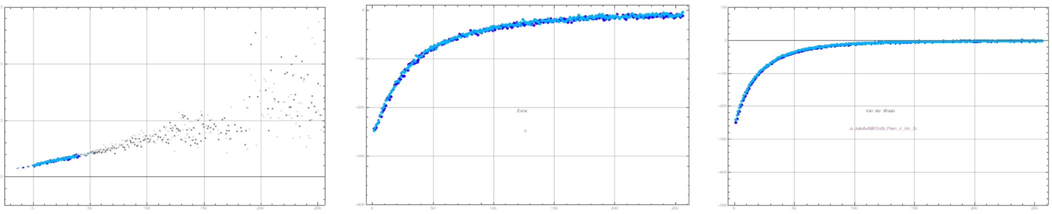

Figure 4.4: Ratio, electrostatic and Van der Waals

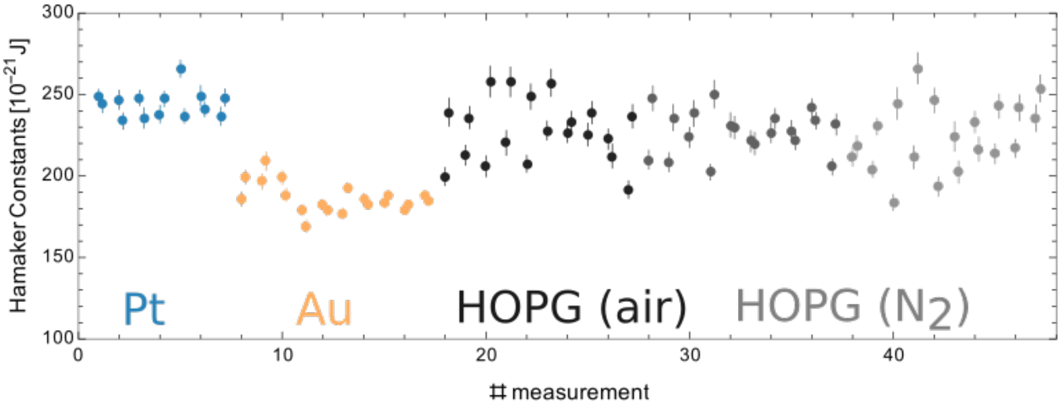

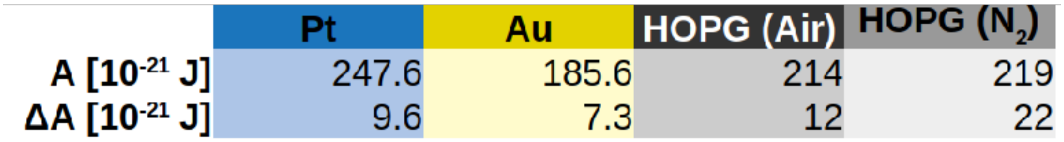

	Pt	Au	HOPG (Air)	HOPG (N_2)
A [10^{-21} J]	247.6	185.6	214	219
ΔA [10^{-21} J]	9.6	7.3	12	22

Figure 4.5

4.4 Discussion

- It was really important for this work to take care of the DAFM technique in order to filter out inconvenient interactions.
- We have proposed a method for calculating the Hamaker constant of conductive materials: metals and semiconductors, since the measurement of the electrostatic interaction is required.
- The Hamaker constant can be determined from a linear regression analysis of the data; with high precision and very low systematic error.
- The method is insensitive to the mechanical properties of the cantilever and the geometry of the tip.

Chapter 5

Characterization of nanoscale contamination adsorbed in air

5.1 Introduction

AFM is a widely used technique in different fields of science, due to its extreme resolution and its high versatility. AFM allows to obtain images of surfaces, of small systems and of adsorbed atoms and molecules on a nanometric, atomic and even sub-atomic scale in environments as different as air, liquids and vacuum. AFM operation is based on the interaction between a sharp tip (the probe) and the sample to be analyzed. To obtain images, this interaction is maintained constant by changing the normal position (z-direction) as the tip is scanned over the surface (lateral, x,y-directions); while in spectroscopy operation, the lateral position is kept constant as the normal position of the sample is varied in order to access material properties ("chemical information", thus the name spectroscopy)3. AFM allows not only the measurement of surface topography, but also the determination of other physical characteristics; in particular electrostatic AFM (EAFM) and magnetic properties. For reliable data acquisition a well-defined and stable tip is essential. It is well known that image resolution and more generally data quality depends critically on the tip geometry as well as on its material properties. Correspondingly, numerous efforts have been devoted to fabricate tips that are well characterized and at the same time as sharp as possible9. On the other hand, even the best tip as fabricated originally may be of limited use if it does not maintain its specified properties during AFM operation10,11

It is generally accepted that tip degradation—either tip wear or tip contamination from the sample—is mainly induced by AFM operation [48, 49, 50]. Tip degradation depends critically on the sample to be analyzed, the medium used for AFM operation, as well as the operation mode. However, a number of works have also emphasized the importance of tip contamination even prior to tip usage. In this context, several groups have investigated the different kind of contamination that may affect the tip: organic contamination from ambient air, metallic pollutants due to the manufacturing processes, as well as contamination induced by the Gel-Pak containers used for chip transport and storage[51, 23]. As a consequence, a variety of cleaning procedures have been proposed to recover the ideal tip as manufactured initially; ranging from less aggressive methods such as washing with sodium dodecyl sulfate (SDS), alcohols like ethanol or acetone[52], ultraviolet (UV)[53] and ozone treatment[54], imaging of gratings[55, 56], heating to evaporate contaminants[57, 58], argon bombardment and even ultrasound; to much more aggressive methods such as piranha solution cleaning[59] and the RCA process[38], both being very successful for removal of organic and metal contamination. We note however that these latter cleaning methods (and maybe even some of the first ones) may modify tip radius and/or its physical and chemical properties.

Finally, almost as important as cleaning is a good characterization of tip properties, in particular the contamination state of the tip. In this context, several methods for tip characterization have been proposed, such as X-ray analysis, Raman spectroscopy, contact angle measurements, scanning and transmission electron microscopy, etc.[60, 61, 62, 63]. We note that usually all these methods require removal of the tip from the AFM setup to some other equipment, which implies on the one hand a significant time effort, and on the other hand the problem related to possible tip change during the transfer process. The ex-situ analysis of the tip may therefore be of limited use to extrapolate how the tip had been during prior AFM data acquisition. Moreover, since the tip may change quite frequently during AFM operation, ex-situ methods may be quite inadequate and unproductive for many AFM experiments. Some methods have been proposed to infer tip properties—in particular the radius—using AFM techniques, which in our opinion is the optimal approach[64, 65, 66, 67].

As discussed in the introduction, AFM is fundamentally based on tip-sample interaction. In this context, we may interpret that the tip is one half of the system, the sample being the other half. Unfortunately, the tip is that half of the system which is not directly seen, making tip characterization using AFM techniques a non-trivial task. To formalize this idea, we recall that within the Derjaguin approximation, the tip-sample force $F_{tip-sample}$ is[41]

$$F_{tip-sample} = 2\pi R w(D) \tag{5.1}$$

where $w(D)$ is the interaction per unit area of two infinite surfaces separated by a distance D and R is the tip radius (more precisely: R is the effective radius of the tip-sample system; $1/R = 1/R_{tip} + 1/R_{surface}$ with R_{tip} tip radius and $R_{surface}$ local surface curvature). Relation 5.1 shows that the tip-sample force is proportional to the tip geometry (described by the tip radius) on the one hand, and by the material properties on the other (described by the surface energy $w(d)$). In the context of the present work we note that relation 5.1 may be understood in the following way: it separates tip-sample interaction into a term describing geometry (radius R) and the term $w(d)$ describing the chemistry of the system.

In the present work, we propose to characterize the tip following two basic ideas. First, we will (indirectly) image the tip by assuming that, to a first approximation, the apex of the tip should have a similar degree of contamination as the rest of the cantilever and of the chip onto which the tip and cantilever are attached. Second, we will assume that by precisely measuring the tip-sample interaction as a function of tip-sample distance we can infer properties related to the surface energy as well as the Contact Potential, and thus to the chemistry of the tip-sample system. We will show that tip contamination severely reduces tip-sample interaction, essentially due to a lower effective Hamaker constant of the tip-sample system. This leads to less interaction signal and thus to a worse signal to noise ratio.

5.2 Experimental methods

5.2.1 AFM data acquisition

Data was acquired using DSFM on a Nanotec Electronica AFM system with a PLL board (bandwidth $\sim 2kHz$), which maintained the cantilever at resonance. Images and spectroscopy were acquired using the frequency as signal for the feedback channel (frequency modulated dynamic scanning force microscopy (FM-DSFM))[22] at small oscillation, which generally implies non-contact operation (so-called attractive regime, for more detail see reference [45]). Tip-sample distance is estimated to be between 5 and 10 nm, ensuring low noise imaging with high spatial resolution, not only of topography but also of electrostatic interaction ($\sim 20nm$). Platinum coated silicon tips ($\nu_0 \sim 70kHz$) with a nominal force constant of $3N/m$ were used. The nominal radius value for tip apex of these probes is specified as $15nm$ by the manufacturer.

5.2.2 AFM imaging

Electrostatic measurements were performed by detecting the frequency shift (and thus the force gradient) induced by an alternating bias between tip and sample (also termed FM-detection of electrostatic force). This frequency shift is

$$\frac{\Delta\nu_{el}(x,y)}{\nu_0} = \frac{C''(d)}{2c_{lever}}\left(U_{bias} - U_{CP}(x,y)\right)^2 \tag{5.2}$$

where $C''(D)$ is the second derivative of the capacitance; ν_0 the free resonance frequency and c_{lever} the spring constant of the cantilever. For a bias voltage $U_{bias} = U_{DC} + U_{AC}\sin\nu_{elec}t$ three frequency components of the electrostatic interaction are obtained from equation 5.2: a direct current (DC) signal, U_{DC}; an alternating current (AC) signal, U_ν, varying with the same frequency as the electrical modulation frequency ν_{elec}; and a third signal, $U_{2\nu}$, varying with twice that frequency [35, 68, 69, 70]. These two signals U_ν and $U_{2\nu}$ are analyzed using lock-in techniques to obtain the electrostatic images electrostatic scanning force microscopy (ESFM) and electrostatic scanning force microscopy at 2 nu (ESFM2); the first is related to the contact potential difference,U_{CP}, between tip and sample and the second to the capacitance of the tip-sample system. To measure contact potencial (CP) images the Kelvin probe microscopy (KPM) technique is used. In this technique the signal ESFM is nullified with an auxiliary feedback system by adjusting the tip voltage, then the voltage applied to the tip is precisely the contact potential, $U_{DC} = U_{CP}$. Frequency detection gives higher spatial resolution as compared to force detection ESFM, in addition, it allows for a correct determination of CP (see, for example, references [71, 45]). An external lock-in amplifier (Signal Recovery 7280 Wide Bandwidth DSP Lock-in Amplifier) was employed for the EAFM and KPM measurements using U_{AC} voltages as low as $U_{AC} \approx 500mV$ at an electrical modulation frequency $\nu_{elec} \approx 7kHz$. Further details of the set-up and EAFM and KPM[35] working operation modes are described elsewhere[45]. WSxM software was used for image processing[72]. Typically a plane filter was applied to topography images; no filter is applied to the electrostatic images.

5.2.3 Multidimensional Spectroscopy: *Interaction Images*.

Multidimensional spectroscopy data is acquired as *interaction images* using the 3D-Mode routine of the WSxM acquisition program[72]. In this kind of spectroscopy data the horizontal axis (fast scan direction) corresponds to a voltage sweep, while the vertical axis (slow scan direction) corresponds to tip-sample distance. The colour scale shows the variation of resonance frequency due to tip-sample interaction as a function of bias voltage and tip-sample distance. Note that, as discussed in more detail elsewhere, for each distance a parabola is obtained that shows a quadratic dependence of the frequency shift with bias, as expected when the AFM system is operated in the non-contact regime. Fitting the experimental data to a parabola, for each (voltage) scan line three parameters are determined: the position of the minimum of each parabola, corresponding to the Contact Potential U_{CP}, the vertical offset of the parabola (measured interaction at the minimum of the parabola) corresponding to the Van der Waals interaction, and finally the curvature of each parabola, which is determined by the capacity, and thus by the strength of electrostatic interaction. The methodology of "interaction imaging" is described in detail in [31].

5.2.4 Sample preparation

For the experiments Platinum coated (on tip-side) Silicon Cantilevers (Olympus OMCL-AC240TM), silicon nitride tip-sharpened (Olympus OMCL-HA100) and All-in-One Platinum coated (on tip-side) Silicon probes (Budget Sensors AIOAl-TL) were utilized. All the experiments have been performed at room temperature and ambient conditions. For cleaning of the cantilevers the RCA process has been used[38, 39].

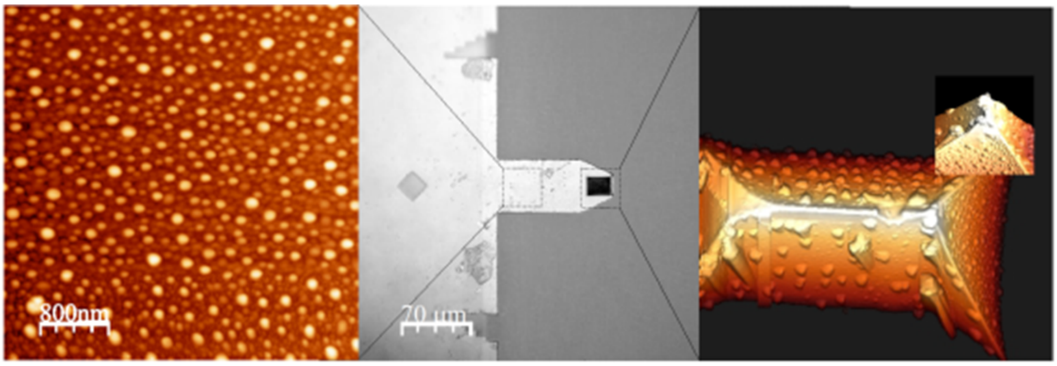

Figure 5.1: AFM images (a, left and c, right) and optical image (1b, middle) of the tip side of an Olympus OMCL-HA-100 AFM cantilever. Image sizes: $36 \times 36\ \mu m^2$ lateral size and $25\ nm$ height scale for the left AFM image (1a) showing the flat region of the cantilever; about $300 \times 300\ \mu m^2$ for the optical image (middle), and $36 \times 36\ \mu m^2$ for the right AFM image showing the flat regions of the cantilever (right). In this latter image, the total height corresponds to about $4\ \mu m$. The dotted squares in the optical image mark the two regions where the AFM images have been acquired.

5.3 Results

5.3.1 Topographic imaging of tip and flat part of a cantilever

Figure 5.1 shows images where the lower side of the cantilever, that is, the side with the sensing tip, has been used as the sample. We have found that tip-sample interaction between the lateral sides of the tip cone may be huge if two plane lateral sides of the tip interact together. In a sense such a tip-probe versus tip-sample system has infinite effective tip radius R giving a huge adhesion force (recall $F_{adh} = 4\pi R\gamma\cos(\phi)$, with surface energy of water and contact angle of water on the material of the tip-sample system, usually the system "wets", then cos 1). In this context we note that during our experiments we have observed (on an optical microscope) how the sample-tip adheres to the sensing-tip and the whole macroscopic sample (tip and chip) is moved as the probe-tip jumps to contact with the sample-tip and the whole system is moved by the scanning motion of the piezoelectric element. In spite of these problems, we have been able to image an AFM cantilever and its tip (figure 5.1), which shows the flat cantilever part (figure 5.1 left), the tip (figure 5.1, right) and an optical image of the whole cantilever (figure 5.1, middle). In the optical image the scan areas corresponding to the two AFM images are marked with two rectangles. The sample cantilever was taken out of the box and imaged without further processing (in particular no cleaning). As can be clearly observed in figure 5.1 the cantilever surface is covered by round islands of typically 50 nm diameter and 10-20 nm height (contact angle of these drop-like particles assuming a spherical surface: about 45). From these topographic images we deduce that the surface of the cantilever is severely contaminated, since the images do not show the characteristic structure of evaporated, multi-crystalline platinum grains. Moreover, as observed in figure 5.1, essentially the same kind of contamination is observed on the flat part of the cantilever and on the sides of the tip cone. Even though we have not been able to image the tip apex at high resolution we believe that our observation supports the hypothesis that if the composition of the whole cantilever is uniform then the contamination observed on the flat part of the cantilever is analogous to the contamination present on its tip. We may assume that the contamination layer behaves like a carpet covering all parts of the cantilever, and in particular the tip apex used as probe in AFM applications. Therefore, if the material of the whole cantilever is uniform the contamination state of the tip can inferred by characterizing the flat part of the cantilever, which is the experimentally much simpler system.

5.3.2 Topography and electrostatic images of cleaned and uncleaned cantilevers: accessing material properties

Topographic images as shown in figure 5.1 are quite valuable if the sample is well controlled. However, in many cases the morphology gives only a limited amount of information with respect to the chemical composition of the sample. Fortunately, AFM provides additional "secondary channels" from which compositional information can be extracted. As discussed in more detail in[45], data can be acquired in the true non-contact regime (nc-DAFM), where only Van der Waals (dispersive) and electrostatic interactions are present. In this work we will assume that the tip-sample system can be described by a metallic tip interacting electrostatically with a metallic sample and that on each metallic surface a thin dielectric film may be adsorbed. In addition, we will assume that the (second derivative of) tip-sample capacitance (see equation 5.3) can be approximated by the expression $C''(d) = \pi\epsilon_0 R/(d + h/epsilon)^2$, where R is the effective tip radius, d the tip-sample distance, h the total thickness of the dielectric films and ϵ their relative dielectric constants[? ?]. For a purely metallic system were the only dielectric is air or vacuum, $h = 0$. The total frequency shift induced by tip-sample interaction is then

$$\frac{\Delta\nu(x,y)}{\nu_0} = \frac{1}{2c_{lever}}\left(\frac{AR}{3d3} + \frac{\pi\epsilon_0 R}{(d+h/\epsilon)^2}\left(U_{bias} - U_{CP}(x,y)\right)^2\right) \tag{5.3}$$

where the first term with the Hamaker constant, A, describes the Van der Waals interaction and the second term describes the electrostatic interaction. We note that the chemical composition of the sample will determine three different parameters in this relation: the Hamaker constant A, the pole of the capacity term and the Contact Potential U_{CP}. All three terms will be used in the present work to infer the composition of the tip-sample system. In particular the Contact Potential between two materials should be quite sensitive to variations of parameters such as the work function, and is widely used to detect adsorption layers, oxide layers, dopant concentration in semiconductors, and even temperature changes, on the sample.

Figure 5.2 shows images of three different experiments where the flat part of the cantilever chip has been analysed in (true) nc-DAFM using and Kelvin Probe Microscopy (KPM), that is, by recording the tip-sample voltage that has to be applied to have Electrostatic Atomic Force Microscopy First Harmonic (EAFM 0. In addition to the topography, also the error signal of the feedback (frequency shift) as well as the Contact Potential and the signal Electrostatic Atomic Force Microscopy Second Harmonic (EAFMare measured simultaneously. The three samples analysed correspond to the surface of platinum-films evaporated onto silicon cantilevers, but with three different state of contamination: one was taken from a box that had been open for first time quite long ago (more than a year) which will be termed uncleaned–old (figure 5.2A, top), another one taken from a freshly open box term uncleaned–new (figure 5.2B, middle) and the last one, termed cleaned (figure 5.2C, bottom), had been cleaned just before imaging using the RCA procedure discussed in the experimental section.

We will first discuss the results obtained on the sample uncleaned–old. As for the case of the cantilever imaged in figure 5.1 the topographic image (Fig2A(a)) shows round islands of approximately 50 nm diameter and 10-20 nm height, which we again associate to surface contamination. We note that although the surface composition of the cantilever imaged in figure 5.1 (material: silicon nitride) and that imaged in figure 5.2A (material: Pt-coated silicon) is very different, the topography of the surfaces looks quite similar. This seems reasonable taking into account that both cantilevers came from a box that had been open long time before the experiments. Therefore, these cantilevers had enough time to be exposed to ambient air (each time a cantilever is extracted from the box) and become severely contaminated.

From the topography image one would conclude that the platinum surface is covered by some contamination (round islands); that is, one would expect two kinds of materials on the surface: the platinum substrate and some other material most probably organic on top of the platinum. Surprisingly, the Contact Potential image is completely homogeneous, which leads to the conclusion that either the islands are completely transparent to the measurement of Contact Potential (more precisely: no charge transfer due to differences in work function between the platinum and the material of the island) or that the platinum surface is covered everywhere by the same material, that is, the Contact Potential image detects the same material on the islands as well as on the flatter part between the islands. Since the Contact Potential image is very sensitive to differences in work function and since it seems unlikely that platinum has the same work function as the (unknown) material of the island, we think that the most logical explanation for the homogeneous

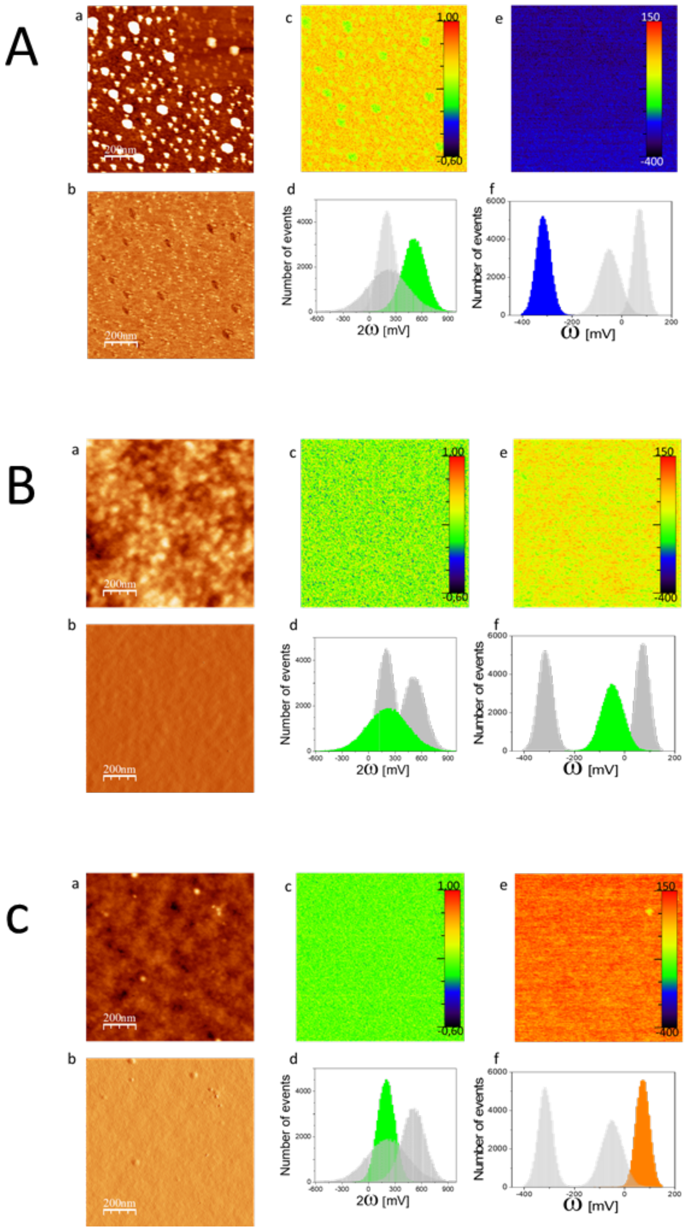

Figure 5.2: Topography (a), error signal (b), capacity data (c) and Contact Potential (e) acquired on the flat part of three platinum coated AFM cantilevers: *uncleaned-old*(top row, A), *uncleaned new* (middle row, B) and *cleaned* (bottom row, C). Lateral image size is $1 \times 1\ nm^2$. Height scale for all topography images is $5\ nm$ (however: right top inset in subfigure Aa is $20\ nm$), -600 to $100\ mV$ for the contact potential image and arbitrary units (output of lock-in amplifier) for the capacity image. The histograms (d) and (f) show the variation of data in the corresponding images above; capacity (c) and contact potential (e), respectively. Note that data is shown in logic order rather than time order, in order to avoid contamination from the sample to the tip. The chronological order in which these images were acquired is therefore: first the sample *uncleaned-new*, then (RCA) *cleaned*, and finally *uncleand old*.

Contact Potential image is the second one: the whole surface is covered by the same material which corresponds to an adsorbed contamination layer. Moreover, this explanation is also supported by results to be discussed below.

As compared to the Contact Potential, the capacity image ($\mathrm{EAFM}_{2\nu}$, figure 5.2A-c) shows a clear contrast between the lower region and the islands. According to equation 5.3 the capacity is $C''(d) \sim (d + h/\epsilon_0)^{-2}$, we therefore interpret that the lower capacity on the islands is due to a larger thickness of the (dielectric) contamination film. Note that if the islands were composed of a conducting material, then h=0 and we would expect no contrast of the capacity $C''(d)$.

Figure 5.2B shows the results obtained for the cantilever of type uncleaned–new which, as discussed above, corresponds to a cantilever which had been taken from a freshly opened cantilever box. In this case, all images topography, Contact Potential and capacity look quite homogeneous. Unfortunately, these homogeneity does not indicate whether the surface is homogeneously clean, or homogeneously contaminated.

Finally, figure 5.2C shows images corresponding to a cantilever cleaned using the RCA method. The topography image is, on a larger scale (200 nm) quite flat showing a small irregular corrugation (5 nm) which is typical of the silicon substrate on which the thin platinum film (nominally 20 nm thickness) is evaporated. On a smaller scale (image not shown) this sample shows the typically rounded structure of the poly crystalline platinum grains (20 nm size). A few higher structures (3 nm) can be recognized in the topographic images. Interestingly only one of these higher structures gives a contrast in the Contact Potential image (-90 mV as compared to 70 mV for the substrate), otherwise the Contact Potential image is completely homogeneous.

5.3.3 Multidimensional AFM Spectroscopy of cleaned an uncleaned cantilevers

To better characterize the tip-sample system, we have acquired multidimensional microscopy data—so-called interaction images—at specific locations of the sample. These interaction images are then processed to separate Van der Waals and electrostatic interactions. For each interaction image three curves are obtained: a Van der Waals interaction $VDW(D)$ curve, the tip-sample capacitance $C(D)$ curve (not shown) and a CP versus distance curve $U_{CP}(d)$. This data is essentially processed as follows: first, a radius R is determined from the capacity curve by fitting each curve to the second term in relation 2, then the Hamaker constant is determined from a fit to the first term in relation 2, that is from the Van der Waals versus distance curve. VdW(d)(see graphs in figure 5.3; more precisely: the product A R is obtained from the fit to. VdW(d), and with the tip radius R from the capacity curve finally the Hamaker constant A is obtained].

Figure 5.3 shows the results of experiments where (topography) AFM imaging is combined with the acquisition of interaction images at well-defined spots. AFM data -topography images and interaction images- are acquired on samples of con-

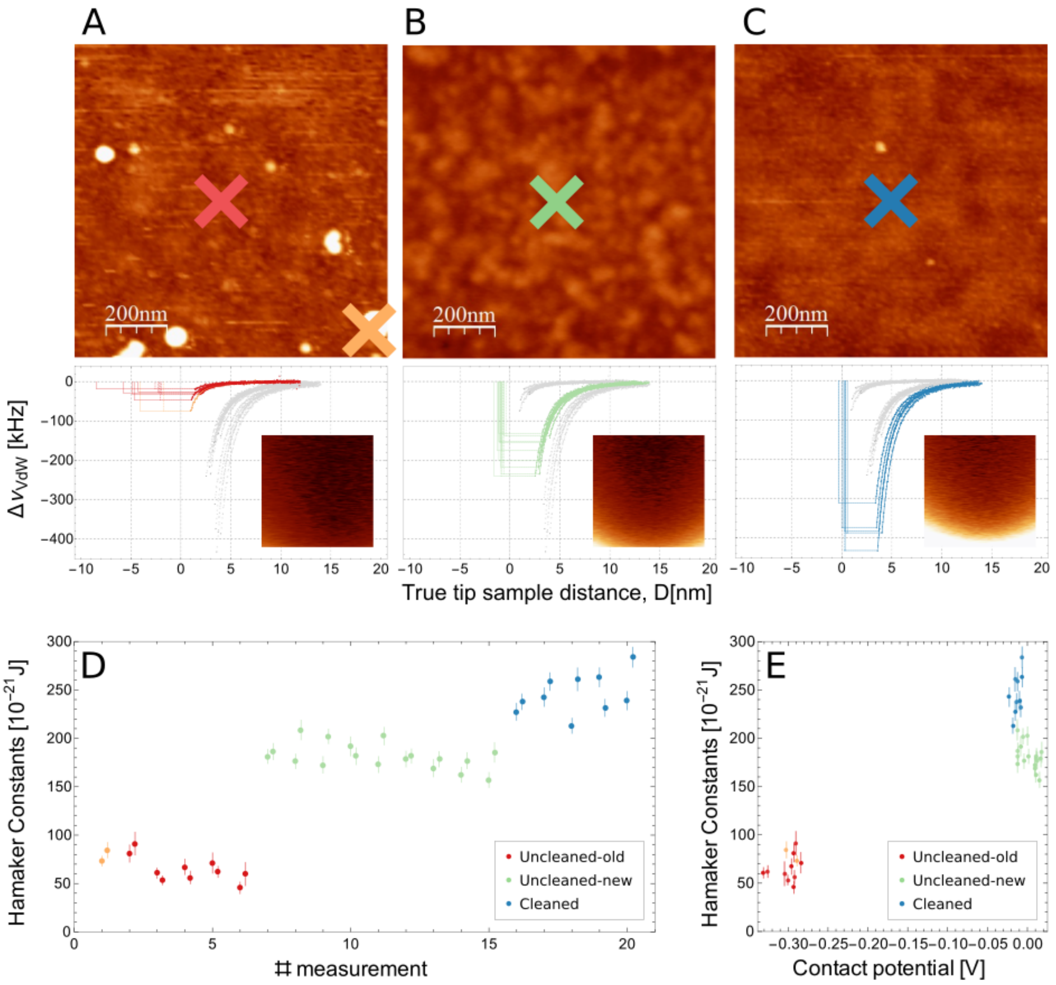

Figure 5.3: Topography images and spectroscopy data at specific locations on three different Pt-coated cantilever chips used as samples. Each chip has a different degree of contamination: *uncleaned-old* (column A, left), *uncleaned-new* (column B, middle), *cleaned* (column C, right). Top row: topography images. Middle row, below the corresponding topographical images: Van der Waals spectroscopy curves $\Delta\nu_{VdW}(d)$ for each sample. The different curves are shown in the color corresponding to the cross in the topographic images above marking the position of the spectroscopy experiment. Note that in each graph all curves are shown, in color those at the position marked in the topographic image above, while all the other curves are shown in gray for easy comparison. The tip-sample distance corresponds to the true tip-sample distance; that is $d = 0$ corresponds to the position of the surface as seen by the Van der Waals interaction. The vertical lines to the left (negative distance) of the experimental $\Delta\nu_{VdW}(d)$ curves in these graphs show the electrostatic pole. The inset in these graphs show one of the interaction images (raw data, total color scale $300\ Hz$, horizontal scan (=fast scan, applied bias voltage) corresponds to $\pm 0.8V$ and the vertical scale (= slow scan, tip-sample distance) to $10\ nm$. The $\Delta\nu_{VdW}(d)$ curves are calculated from these interaction images. Bottom row: Hamaker constant (D) and Hamaker constant versus Contact Potential diagram (E) for all spectroscopy experiments acquired at the positions shown in the different topographic images. The colors of the data points correspond to the positions of the different data sets (and samples) marked in the topographic images.

Sample	Hamaker constant $A[10^{-21}J]$	Contact potential $U_{CP}[V]$	Dielectric thickness $h/\epsilon_0[nm]$
uncleaned-old	66 ± 8	-0.30 ± 0.02	5 ± 8
uncleaned-new	180 ± 12	0.00 ± 0.01	1 ± 1
cleaned	245 ± 20	-0.02 ± 0.01	0.0 ± 0.5

Table 5.1: The corresponding results from the spectroscopic experiments are summarized in this table.

tamination type uncleaned-old, uncleaned-new, and cleaned (see discussion above). On each spot, several interaction images are obtained, the corresponding results are shown in figure 5.3. We perform 20 spectroscopy experiments, for each single experiment two data sets are acquired, processed and shown: one corresponding to an approach cycle and another one to a retraction cycle of a spectroscopy experiment. Data sets n=1-6 are obtained on an uncleaned old, data sets n=7-15 on an uncleaned-new and data sets n=16-20 on a (RCA) cleaned cantilever. From each spectroscopy experiment, the Hamaker constant A, the contact potential CP and the thickness of the dielectric layer h/ϵ_0 are determined; the corresonding mean values of these parameters determined for the three different samples are listed in table 5.1.

All data is acquired in the true non-contact regime, that is, the tip-sample system does neither enter mechanical contact, nor are liquid necks formed (see reference[45]). In fact, the oscillation amplitude during all experiments was the free oscillation amplitude, which implies no snap to contact nor sudden decrease of oscillation amplitude due to formation of liquid necks (see discussion and figure 4 in reference[31]). Correspondingly the data is very reproducible and we observe a clear difference between data acquired on the samples with different degree of contamination. Clearly, the difference of the values obtained for the Hamaker constant, the Contact Potential and the thickness of the dielectric layer obtained for each individual spectroscopy experiment is smaller than the difference of these values obtained on the different cantilevers. This is most easily visualised in the Hamaker constant versus Contact Potential plot (5.3E, bottom right) where the measurements can clearly and uniquely be attributed to the three different groups, corresponding to the cantilevers of type uncleaned-old, uncleaned-new and cleaned. We are therefore able to detect the variation of the Hamaker constant, as well as of the Contact Potential due to the chemical differences induced by the contamination in the tip-sample system.

5.4 Conclusions

The present work describes our effort to shed light on the issue of nanoscale contamination on surfaces, and in particular within an AFM tip-sample system; used here on the one hand as a model system, and on the other as a characterization instrument. It is generally accepted that contamination must be present when working in ambient conditions; otherwise the extreme effort to work in UHV conditions would not make any sense. However, in general the precise way in which this contamination affects many surface processes is neither understood in detail nor well controlled. In fact, in our opinion, this issue is often just ignored, in particular in the AFM community. Many more AFM related measurements are performed in ambient conditions as compared to UHV, and AFM in ambient conditions has become a fundamental and widely used tool for nanoscale research in material science, biology and medicine, physics, chemistry but also engineering and environmental sciences. We are therefore convinced that this issue of quantification of surface contamination in ambient conditions is not merely a "technical issue" related only to AFM operation, but a topic of much broader relevance.

From our work we conclude that not only contamination of the tip, but also that on the sample surface is quite difficult to visualize and detect, but is nevertheless quite important, and significantly determines AFM results and interpretation. In the present work we have shown how the presence of contamination in the tip-sample system can be detected and quantified using only AFM techniques. The methodology presented allows for simple in–situ characterization and checking of the tip-sample system, without needing to remove the tip and/or the sample from the AFM set-up.

To infer the contamination of the tip we have adopted the assumption that, if the whole cantilever is composed of the same material then the contamination should cover the tip apex, the tip and the flat part of the cantilever in a similar way. This assumption should be quite correct if the contamination layer is thinner than the radius of curvature of the tip, typically 20 nm, which should be the case in most AFM experiments. Taking two equivalent cantilevers and using one as probe and the other one as sample allows to observe and measure the properties of the tip, since in a sense, the tip is looking at the (statistically) equivalent sample system. Within the Derjaguin Approximation (see relation 1) the chemistry of the tip-sample system is described by the surface energy w(d) and we interpret that for the Pt-Pt tip-sample system used in the present work this surface energy term is due to twice the same system: in our case Pt with a (dielectric) contamination layer.

To validate our working assumption, we have first imaged the tip and the flat cantilever regions of a cantilever taken from a typical enclosing box. As discussed previously in the literature, we find a high degree of contamination on the cantilevers and –more importantly in the present context– we observe that this contamination layer covers in a similar way the tip and the flat part of the cantilever (figure 5.1). In the second experiment we have used imaging of topography as well as of electrostatic properties to characterize cantilevers used as a sample. We have imaged three tip-sample systems with different degree of contamination, and find different electrostatic response of the capacity signal and of the Contact Potential (figure 5.2). Unfortunately, the data obtained from these images is not completely conclusive: a Contact Potential difference near zero may indicate that the tip and the sample is either clean, or that both are contaminated in a similar way. Using multidimensional spectroscopy techniques (interaction imaging) and advanced data processing we are capable to locally determine the effective Hamaker constant of the tip-sample system, and we find that this Hamaker constant is very sensitive to the contamination state of the tip-sample system (figure 5.3). Finally, we note that the methodology of acquisition and processing of interaction imaging is independent of the tip radius, a fundamental parameter for tip-sample interaction (see the Derjaguin approximation, relation 1) that is often quite difficult to obtain precisely. In fact, we believe the precision and robustness of our methodology is due to the fact that its results do not depend on the tip size.

We propose the method presented in this work as a simple, very precise and sensitive, and –very important– as an in-situ characterization of the AFM tip-sample system. Moreover, we believe that our methodology is particularly suited for AFM since it is based on determining the effect of contamination on the tip-sample interaction, which is the fundamental physical property that determines AFM operation. That is, as compared to other non-AFM based techniques for the determination of contamination, our method detects the contamination that particularly affects tip-sample interaction, and that will therefore have an important effect on AFM data acquisition and data interpretation. In the future this method will be easily extended to improve nanoscale material characterization in the following way: once the tip is known to be clean, the properties of an unknown surface can be characterized as discussed in the present work precisely because the tip side is clean and well controlled and not anymore an unknown parameter of the system. Only then the measured properties of the tip-sample system can be uniquely attributed to the sample. In the future we propose to further develop the technique presented here to make AFM a truly quantitative nanoscale Material Science characterization tool to characterize—among others—the degree of nanoscale contamination on surfaces in ambient conditions.

Conclusions

In this study, an advanced force spectroscopy technique has been developed and applied to obtain specific material properties. With this technique it is possible to accurately distinguish and characterize electrostatic and dispersion interactions as well as to obtain material-related properties such as CPD or the Hamaker constant. Therefore, by applying this technique, it is possible to characterize metal and semiconductor surfaces using the Hamaker constant and the CPD. An important part of the methodology is based on data processing that has been developed specifically for that porpoise. This processing is considered self important and definitely novel in the AFM community.

In addition, the development of this technique has meant, in parallel, an advance in the understanding of the interaction between the tip and the sample in AFM that has led to a reclassification of the modes of measurement that we consider it will be important to take into account in future studies to improve the collection of qualitative results with AFM techniques. Among the community who operates the AFM in air, it is common to classify modes of measurement into attractive or repulsive regimes or into contact and non-contact modes. One of the most solid conclusions revealed by this work is that those of us who work with AFM in air have to take a further step in our quest to find quantitative and reproducible results as it will be show in the following chapters.

For this purpose, it is essential to have a well-defined interaction between the tip and the sample. Non-conservative capillary forces created by the capillary bridges that form and break between the tip and the sample when the distance is small enough introduce non-linearity that makes it difficult to collect data and analyze them with well-defined models.

For this reason we introduce what we call the **true non-contact mode** (to differentiate it from the traditional non-contact mode) as a measurement mode in AFM, generally operated in frequency modulation, characterized by small amplitudes of oscillation at a sufficient distance from the sample to prevent the formation of liquid necks between the tip and the sample. Only in this case, the only contributions to the total interaction between tip and sample are the electrostatic and van der waals interactions.

With this same purpose, it has been seen and demonstrated that it is important to have well-defined surfaces in air and that pollution is a factor to take into account when interpreting the results. From our work we conclude that not only contamination of the tip, but also that on the sample surface is quite difficult to visualize and detect, but is nevertheless quite important, and significantly determines AFM results and interpretation. In the present work we have shown how the presence of contamination in the tip-sample system can be detected and quantified using only AFM techniques. The methodology presented allows for simple in–situ characterization and checking of the tip-sample system, without needing to remove the tip and/or the sample from the AFM set-up.

Bibliography

[1] G. Binnig, H. Rohrer, Ch. Gerber, and E. Weibel. Surface Studies by Scanning Tunneling Microscopy. *Physical Review Letters*, 49(1):57–61, July 1982. doi: 10.1103/PhysRevLett.49.57. URL https://link.aps.org/doi/10.1103/PhysRevLett.49.57.

[2] G. Binnig, H. Rohrer, Ch. Gerber, and E. Weibel. 7x7 Reconstruction on Si(111) Resolved in Real Space. *Physical Review Letters*, 50(2):120–123, January 1983. doi: 10.1103/PhysRevLett.50.120. URL https://link.aps.org/doi/10.1103/PhysRevLett.50.120.

[3] O. K. Binnig, H. Rohrer, Ch. Gerber, and E. Stoll. Real-space observation of the reconstruction of Au(100). *Surface Science*, 144(2):321–335, September 1984. ISSN 0039-6028. doi: 10.1016/0039-6028(84)90104-3. URL http://www.sciencedirect.com/science/article/pii/0039602884901043.

[4] A. M. Baró, G. Binnig, H. Rohrer, Ch. Gerber, E. Stoll, A. Baratoff, and F. Salvan. Real-Space Observation of the 2x1 Structure of Chemisorbed Oxygen on Ni(110) by Scanning Tunneling Microscopy. *Physical Review Letters*, 52(15):1304–1307, April 1984. doi: 10.1103/PhysRevLett.52.1304. URL https://link.aps.org/doi/10.1103/PhysRevLett.52.1304.

[5] U. Dürig, J. K. Gimzewski, and D. W. Pohl. Experimental Observation of Forces Acting during Scanning Tunneling Microscopy. *Phys. Rev. Lett.*, 57(19):2403–2406, November 1986. doi: 10.1103/PhysRevLett.57.2403.

[6] G. Binnig, C. F. Quate, and Ch. Gerber. Atomic Force Microscope. *Physical Review Letters*, 56(9):930–933, March 1986. doi: 10.1103/PhysRevLett.56.930. URL https://link.aps.org/doi/10.1103/PhysRevLett.56.930.

[7] H. Hertz. Ueber die Berührung fester elastischer Körper. *Journal fur die Reine und Angewandte Mathematik*, 1882(92):156–171, 1882. doi: 10.1515/crll.1882.92.156.

[8] L.D. Landau & E.M. Lifshitz. *Theory of Elasticity*. URL http://archive.org/details/TheoryOfElasticity.

[9] Pierre-Gilles de Gennes, Francoise Brochard-Wyart, and David Quere. *Capillarity and Wetting Phenomena: Drops, Bubbles, Pearls, Waves*. Springer Science & Business Media, 2004. ISBN 978-0-387-00592-8.

[10] HC Hamaker. The London—van der Waals attraction between spherical particles. *physica*, 4(10):1058–1072, 1937.

[11] Uwe Hartmann. Magnetic force microscopy. *Advanced Materials*, 2 (11):550–552, November 1990. ISSN 0935-9648, 1521-4095. doi: 10.1002/adma.19900021110. URL http://doi.wiley.com/10.1002/adma.19900021110.

[12] Yves Martin, David W. Abraham, and H. Kumar Wickramasinghe. High-resolution capacitance measurement and potentiometry by force microscopy. *Applied Physics Letters*, 52(13):1103–1105, March 1988. ISSN 0003-6951. doi: 10.1063/1.99224. URL https://aip.scitation.org/doi/abs/10.1063/1.99224.

[13] T. Göddenhenrich, H. Lemke, M. Mück, U. Hartmann, and C. Heiden. Probe calibration in magnetic force microscopy. *Applied Physics Letters*, 57(24): 2612–2614, December 1990. ISSN 0003-6951. doi: 10.1063/1.103827. URL https://aip.scitation.org/doi/abs/10.1063/1.103827.

[14] A. Moser, H. J. Hug, I. Parashikov, B. Stiefel, O. Fritz, H. Thomas, A. Baratoff, H.-J. Güntherodt, and P. Chaudhari. Observation of Single Vortices Condensed into a Vortex-Glass Phase by Magnetic Force Microscopy. *Physical Review Letters*, 74(10):1847–1850, March 1995. doi: 10.1103/PhysRevLett.74.1847. URL https://link.aps.org/doi/10.1103/PhysRevLett.74.1847.

[15] Steffen Porthun, Leon Abelmann, and Cock Lodder. Magnetic force microscopy of thin film media for high density magnetic recording. *Journal of Magnetism and Magnetic Materials*, 182(1):238–273, February 1998. ISSN 0304-8853. doi: 10.1016/S0304-8853(97)01010-X. URL http://www.sciencedirect.com/science/article/pii/S030488539701010X.

[16] Ernst Meyer, Hans Josef Hug, and Roland Bennewitz. *Scanning Probe Microscopy: The Lab on a Tip*. Springer Science & Business Media, 2004. ISBN 978-3-540-43180-0.

[17] M. Saint Jean, S. Hudlet, C. Guthmann, and J. Berger. Van der Waals and capacitive forces in atomic force microscopies. *Journal of Applied Physics*, 86(9):5245–5248, October 1999. ISSN 0021-8979. doi: 10.1063/1.371506. URL https://aip.scitation.org/doi/abs/10.1063/1.371506.

[18] PID controller, October 2018. URL https://en.wikipedia.org/w/index.php?title=PID_controller&oldid=862644580. Page Version ID: 862644580.

[19] Walter C. Michels and Norma L. Curtis. A Pentode Lock-In Amplifier of High Frequency Selectivity. *Review of Scientific Instruments*, 12(9):444–447,

September 1941. ISSN 0034-6748. doi: 10.1063/1.1769919. URL https://aip.scitation.org/doi/abs/10.1063/1.1769919.

[20] Lock In Amplifier - SR830 and SR810. URL https://www.thinksrs.com/products/sr810830.html.

[21] Ricardo Garcia and Ruben Perez. Dynamic atomic force microscopy methods. *Surface Science Reports*, 47(6):197–301, September 2002. ISSN 0167-5729. doi: 10.1016/S0167-5729(02)00077-8. URL http://www.sciencedirect.com/science/article/pii/S0167572902000778.

[22] T. R. Albrecht, P. Grütter, D. Horne, and D. Rugar. Frequency modulation detection using high-Q cantilevers for enhanced force microscope sensitivity. *Journal of Applied Physics*, 69(2):668–673, January 1991. ISSN 0021-8979. doi: 10.1063/1.347347. URL http://aip.scitation.org/doi/abs/10.1063/1.347347.

[23] Franz J. Giessibl. Atomic Resolution of the Silicon (111)-(7x7) Surface by Atomic Force Microscopy. *Science*, 267(5194):68–71, January 1995. ISSN 0036-8075, 1095-9203. doi: 10.1126/science.267.5194.68. URL http://science.sciencemag.org/content/267/5194/68.

[24] Yasuhiro Sugawara, Masahiro Ohta, Hitoshi Ueyama, and Seizo Morita. Defect Motion on an InP(110) Surface Observed with Noncontact Atomic Force Microscopy. *Science*, 270(5242):1646–1648, December 1995. ISSN 0036-8075, 1095-9203. doi: 10.1126/science.270.5242.1646. URL http://science.sciencemag.org/content/270/5242/1646.

[25] Shin Kitamura and Masashi Iwatsuki. Observation of 7x7 Reconstructed Structure on the Silicon (111) Surface using Ultrahigh Vacuum Noncontact Atomic Force Microscopy. *Japanese Journal of Applied Physics*, 34(1B):L145, January 1995. ISSN 1347-4065. doi: 10.1143/JJAP.34.L145. URL http://iopscience.iop.org/article/10.1143/JJAP.34.L145/meta.

[26] Y. Maeda, T. Matsumoto, and T. Kawai. Observation of single- and double-stranded DNA using non-contact atomic force microscopy. *Applied Surface Science*, 140(3):400–405, February 1999. ISSN 0169-4332. doi: 10.1016/S0169-4332(98)00562-5. URL http://www.sciencedirect.com/science/article/pii/S0169433298005625.

[27] Yongho Seo, Hwansung Choe, and Wonho Jhe. Atomic-resolution noncontact atomic force microscopy in air. *Applied Physics Letters*, 83(9):1860–1862, August 2003. ISSN 0003-6951. doi: 10.1063/1.1606493. URL https://aip.scitation.org/doi/abs/10.1063/1.1606493.

[28] Takeshi Fukuma, Kei Kobayashi, Kazumi Matsushige, and Hirofumi Yamada. True atomic resolution in liquid by frequency-modulation atomic force mi-

croscopy. *Applied Physics Letters*, 87(3):034101, July 2005. ISSN 0003-6951. doi: 10.1063/1.1999856. URL https://aip.scitation.org/doi/abs/10.1063/1.1999856.

[29] F. Mugele, T. Becker, R. Nikopoulos, M. Kohonen, and S. Herminghaus. Capillarity at the nanoscale: an AFM view. *Journal of Adhesion Science and Technology*, 16(7):951–964, January 2002. ISSN 0169-4243. doi: 10.1163/156856102760136490. URL https://doi.org/10.1163/156856102760136490.

[30] Zheng Wei and Ya-Pu Zhao. Growth of liquid bridge in AFM. *Journal of Physics D: Applied Physics*, 40(14):4368, 2007. ISSN 0022-3727. doi: 10.1088/0022-3727/40/14/036. URL http://stacks.iop.org/0022-3727/40/i=14/a=036.

[31] Elisa Palacios-Lidón and Jaime Colchero. Quantitative analysis of tip–sample interaction in non-contact scanning force spectroscopy. *Nanotechnology*, 17 (21):5491, 2006. ISSN 0957-4484. doi: 10.1088/0957-4484/17/21/033. URL http://stacks.iop.org/0957-4484/17/i=21/a=033.

[32] Lord Kelvin. V. Contact electricity of metals. *The London, Edinburgh, and Dublin Philosophical Magazine and Journal of Science*, 46(278):82–120, July 1898. ISSN 1941-5982. doi: 10.1080/14786449808621172. URL https://doi.org/10.1080/14786449808621172.

[33] W. A. Zisman. A new method of measuring contact potential differences in metals. *Review of Scientific Instruments*, 3(7):367–370, July 1932. ISSN 0034-6748. doi: 10.1063/1.1748947. URL https://aip.scitation.org/doi/abs/10.1063/1.1748947.

[34] J. M. R. Weaver and David W. Abraham. High resolution atomic force microscopy potentiometry. *Journal of Vacuum Science & Technology B: Microelectronics and Nanometer Structures Processing, Measurement, and Phenomena*, 9(3):1559–1561, May 1991. ISSN 1071-1023. doi: 10.1116/1.585423. URL https://avs.scitation.org/doi/abs/10.1116/1.585423.

[35] M. Nonnenmacher, M. P. O'Boyle, and H. K. Wickramasinghe. Kelvin probe force microscopy. *Applied Physics Letters*, 58(25):2921–2923, June 1991. ISSN 0003-6951. doi: 10.1063/1.105227. URL https://aip.scitation.org/doi/abs/10.1063/1.105227.

[36] Álvaro San Paulo Hernando. *Dinámica de la microscopía de fuerzas con modulación de amplitud descripción teórica e implicaciones experimentales*. PhD thesis, Universidad Autónoma de Madrid, 2002.

[37] Juan Francisco González Martínez. *Explorando los límites de la microscopía de fuerzas: ruido térmico y ruido en la interacción punta-muestra*. PhD thesis, Universidad de Murcia, 2015.

[38] W. Kern. Cleaning solutions based on hydrogen peroxide for use in silicon semiconductor technology. *RCA Review*, 31:187–206, 1970. URL https://ci.nii.ac.jp/naid/10003367909.

[39] Werner Kern. The Evolution of Silicon Wafer Cleaning Technology. *Journal of The Electrochemical Society*, 137(6):1887–1892, June 1990. ISSN 0013-4651, 1945-7111. doi: 10.1149/1.2086825. URL http://jes.ecsdl.org/content/137/6/1887.

[40] B. Derjaguin. Untersuchungen über die Reibung und Adhäsion, IV: Theorie des Anhaftens kleiner Teilchen. *Kolloid-Zeitschrift*, 69(2):155–164, November 1934. ISSN 0303-402X, 1435-1536. doi: 10.1007/BF01433225. URL http://link.springer.com/10.1007/BF01433225.

[41] Jacob N. Israelachvili. *Intermolecular and Surface Forces, Third Edition*. Academic Press, Amsterdam, 3 edition edition, June 2011. ISBN 978-0-12-391927-4.

[42] C. Argento and R. H. French. Parametric tip model and force–distance relation for Hamaker constant determination from atomic force microscopy. *Journal of Applied Physics*, 80(11):6081–6090, December 1996. ISSN 0021-8979. doi: 10.1063/1.363680. URL https://aip.scitation.org/doi/abs/10.1063/1.363680.

[43] EM Lifshitz. The theory of molecular attractive forces between solids. *Sov. Phys. JETP*, 2:73, 1956.

[44] Igor Ekhiel'evich Dzyaloshinskii, EM Lifshitz, and Lev Petrovich Pitaevskii. General theory of van der Waals's forces. *Physics-Uspekhi*, 4(2):153–176, 1961.

[45] E. Palacios-Lidón, B. Pérez-García, and J. Colchero. Enhancing dynamic scanning force microscopy in air: as close as possible. *Nanotechnology*, 20 (8):085707, 2009. ISSN 0957-4484. doi: 10.1088/0957-4484/20/8/085707. URL http://stacks.iop.org/0957-4484/20/i=8/a=085707.

[46] M. Guggisberg, M. Bammerlin, Ch. Loppacher, O. Pfeiffer, A. Abdurixit, V. Barwich, R. Bennewitz, A. Baratoff, E. Meyer, and H.-J. Güntherodt. Separation of interactions by noncontact force microscopy. *Physical Review B*, 61(16):11151–11155, April 2000. doi: 10.1103/PhysRevB.61.11151. URL https://link.aps.org/doi/10.1103/PhysRevB.61.11151.

[47] Jun Hu, Xu-Dong Xiao, and Miquel Salmeron. Scanning polarization force microscopy: A technique for imaging liquids and weakly adsorbed layers. *Applied Physics Letters*, 67(4):476–478, July 1995. ISSN 0003-6951. doi: 10.1063/1.114541. URL https://aip.scitation.org/doi/abs/10.1063/1.114541.

[48] T. R. Albrecht, S. Akamine, T. E. Carver, and C. F. Quate. Microfabrication of cantilever styli for the atomic force microscope. *Journal of Vacuum Science & Technology A: Vacuum, Surfaces, and Films*, 8(4):3386–3396, July 1990. ISSN 0734-2101. doi: 10.1116/1.576520. URL https://avs.scitation.org/doi/abs/10.1116/1.576520.

[49] Koo-Hyun Chung, Yong-Ha Lee, and Dae-Eun Kim. Characteristics of fracture during the approach process and wear mechanism of a silicon AFM tip. *Ultramicroscopy*, 102(2):161–171, January 2005. ISSN 0304-3991. doi: 10.1016/j.ultramic.2004.09.009. URL http://www.sciencedirect.com/science/article/pii/S0304399104001810.

[50] H.-Y. Nie, M. J. Walzak, and N. S. McIntyre. Use of biaxially oriented polypropylene film for evaluating and cleaning contaminated atomic force microscopy probe tips: An application to blind tip reconstruction. *Review of Scientific Instruments*, 73(11):3831–3836, October 2002. ISSN 0034-6748. doi: 10.1063/1.1510554. URL https://aip.scitation.org/doi/abs/10.1063/1.1510554.

[51] Yu-Shiu Lo, Neil D. Huefner, Winter S. Chan, Paul Dryden, Birgit Hagenhoff, and Thomas P. Beebe. Organic and Inorganic Contamination on Commercial AFM Cantilevers. *Langmuir*, 15(19):6522–6526, September 1999. ISSN 0743-7463. doi: 10.1021/la990371x. URL https://doi.org/10.1021/la990371x.

[52] Zhenzhen Lu, Qingxia Liu, Zhenghe Xu, and Hongbo Zeng. Probing Anisotropic Surface Properties of Molybdenite by Direct Force Measurements. *Langmuir*, 31(42):11409–11418, October 2015. ISSN 0743-7463. doi: 10.1021/acs.langmuir.5b02678. URL https://doi.org/10.1021/acs.langmuir.5b02678.

[53] S. M. R. Akrami, H. Nakayachi, T. Watanabe-Nakayama, H. Asakawa, and T. Fukuma. Significant improvements in stability and reproducibility of atomic-scale atomic force microscopy in liquid. *Nanotechnology*, 25(45): 455701, 2014. ISSN 0957-4484. doi: 10.1088/0957-4484/25/45/455701. URL http://stacks.iop.org/0957-4484/25/i=45/a=455701.

[54] Yoh Okabe, Manabu Furugori, Yuki Tani, Uichi Akiba, and Masamichi Fujihira. Chemical force microscopy of microcontact-printed self-assembled monolayers by pulsed-force-mode atomic force microscopy. *Ultramicroscopy*, 82(1): 203–212, February 2000. ISSN 0304-3991. doi: 10.1016/S0304-3991(99)

00143-6. URL http://www.sciencedirect.com/science/article/pii/S0304399199001436.

[55] Yang Gan and George V. Franks. Cleaning AFM colloidal probes by mechanically scrubbing with supersharp "brushes". *Ultramicroscopy*, 109(8):1061–1065, July 2009. ISSN 0304-3991. doi: 10.1016/j.ultramic.2009.03.019. URL http://www.sciencedirect.com/science/article/pii/S0304399109000898.

[56] Shi Bin, Zhang Dongxian, Zhang Haijun, and Sang Qing. Atomic force microscope tip cleaning by using gratings as micro-washboards. *Microscopy Research and Technique*, 76(11):1131–1134, September 2013. ISSN 1059-910X. doi: 10.1002/jemt.22276. URL https://onlinelibrary.wiley.com/doi/10.1002/jemt.22276.

[57] Masahiko Tomitori and Toyoko Arai. Tip cleaning and sharpening processes for noncontact atomic force microscope in ultrahigh vacuum. *Applied Surface Science*, 140(3):432–438, February 1999. ISSN 0169-4332. doi: 10.1016/S0169-4332(98)00569-8. URL http://www.sciencedirect.com/science/article/pii/S0169433298005698.

[58] K. Q. Xu, H. R. Zeng, H. Z. Yu, K. Y. Zhao, G. R. Li, J. Q. Song, X. Shi, and L. D. Chen. Ultrahigh resolution characterizing nanoscale Seebeck coefficient via the heated, conductive AFM probe. *Applied Physics A*, 118(1):57–61, November 2014. ISSN 0947-8396, 1432-0630. doi: 10.1007/s00339-014-8891-4. URL http://link.springer.com/article/10.1007/s00339-014-8891-4.

[59] L. Sirghi, O. Kylián, D. Gilliland, G. Ceccone, and F. Rossi. Cleaning and Hydrophilization of Atomic Force Microscopy Silicon Probes. *The Journal of Physical Chemistry B*, 110(51):25975–25981, December 2006. ISSN 1520-6106. doi: 10.1021/jp063327g. URL https://doi.org/10.1021/jp063327g.

[60] Bogdan C. Donose, Elena Taran, Ivan U. Vakarelski, Hiroyuki Shinto, and Ko Higashitani. Effects of cleaning procedures of silica wafers on their friction characteristics. *Journal of Colloid and Interface Science*, 299(1):233–237, July 2006. ISSN 0021-9797. doi: 10.1016/j.jcis.2006.01.044. URL http://www.sciencedirect.com/science/article/pii/S0021979706000518.

[61] T. Arai and M. Tomitori. Removal of contamination and oxide layers from UHV-AFM tips. *Applied Physics A*, 66(1):S319–S323, March 1998. ISSN 0947-8396, 1432-0630. doi: 10.1007/s003390051154. URL https://link.springer.com/article/10.1007/s003390051154.

[62] Lisa Henke, Noemi Nagy, and Ulrich J. Krull. An AFM determination of the effects on surface roughness caused by cleaning of fused silica and

glass substrates in the process of optical biosensor preparation. *Biosensors and Bioelectronics*, 17(6):547–555, June 2002. ISSN 0956-5663. doi: 10.1016/S0956-5663(02)00012-X. URL http://www.sciencedirect.com/science/article/pii/S095656630200012X.

[63] Keunhan Park, Jungchul Lee, Rohit Bhargava, and William P. King. Routine Femtogram-Level Chemical Analyses Using Vibrational Spectroscopy and Self-Cleaning Scanning Probe Microscopy Tips. *Analytical Chemistry*, 80(9):3221–3228, May 2008. ISSN 0003-2700. doi: 10.1021/ac702423c. URL https://doi.org/10.1021/ac702423c.

[64] Killgore Jason P., Geiss Roy H., and Hurley Donna C. Continuous Measurement of Atomic Force Microscope Tip Wear by Contact Resonance Force Microscopy. *Small*, 7(8):1018–1022, April 2011. ISSN 1613-6810. doi: 10.1002/smll.201002116. URL https://onlinelibrary.wiley.com/doi/full/10.1002/smll.201002116.

[65] Sergio Santos, Li Guang, Tewfik Souier, Karim Gadelrab, Matteo Chiesa, and Neil H. Thomson. A method to provide rapid in situ determination of tip radius in dynamic atomic force microscopy. *Review of Scientific Instruments*, 83(4):043707, April 2012. ISSN 0034-6748. doi: 10.1063/1.4704376. URL https://aip.scitation.org/doi/abs/10.1063/1.4704376.

[66] J. Fraxedas, F. Pérez-Murano, F. Gramazio, M. Lorenzoni, E. Rull Trinidad, and U. Staufer. Continuous monitoring of tip radius during atomic force microscopy imaging. In *Scanning Microscopies 2015*, volume 9636, page 96360O. International Society for Optics and Photonics, October 2015. doi: 10.1117/12.2196951. URL https://www.spiedigitallibrary.org/conference-proceedings-of-spie/9636/96360O/Continuous-monitoring-of-tip-radius-during-atomic-force-microscopy-imaging/10.1117/12.2196951.short.

[67] Federico Gramazio, Matteo Lorenzoni, Francesc Pérez-Murano, Enrique Rull Trinidad, Urs Staufer, and Jordi Fraxedas. Functional dependence of resonant harmonics on nanomechanical parameters in dynamic mode atomic force microscopy. *Beilstein Journal of Nanotechnology*, 8:883–891, April 2017. ISSN 2190-4286. doi: 10.3762/bjnano.8.90. URL https://www.ncbi.nlm.nih.gov/pmc/articles/PMC5405692/.

[68] C. Schönenberger and S. F. Alvarado. Observation of single charge carriers by force microscopy. *Physical Review Letters*, 65(25):3162–3164, December 1990. doi: 10.1103/PhysRevLett.65.3162. URL https://link.aps.org/doi/10.1103/PhysRevLett.65.3162.

[69] Wilhelm Melitz, Jian Shen, Andrew C. Kummel, and Sangyeob Lee. Kelvin probe force microscopy and its application. *Surface Science Reports*, 66(1):1–27, January 2011. ISSN 0167-5729. doi: 10.1016/j.surfrep.2010.

10.001. URL http://www.sciencedirect.com/science/article/pii/S0167572910000841.

[70] Sascha Sadewasser and Thilo Glatzel. *Kelvin Probe Force Microscopy: From Single Charge Detection to Device Characterization*. Springer, March 2018. ISBN 978-3-319-75687-5. Google-Books-ID: C5BQDwAAQBAJ.

[71] J. Colchero, A. Gil, and A. M. Baró. Resolution enhancement and improved data interpretation in electrostatic force microscopy. *Physical Review B*, 64 (24):245403, November 2001. doi: 10.1103/PhysRevB.64.245403. URL http://link.aps.org/doi/10.1103/PhysRevB.64.245403.

[72] I. Horcas, R. Fernández, J. M. Gómez-Rodríguez, J. Colchero, J. Gómez-Herrero, and A. M. Baro. WSXM: A software for scanning probe microscopy and a tool for nanotechnology. *Review of Scientific Instruments*, 78(1): 013705, January 2007. ISSN 0034-6748. doi: 10.1063/1.2432410. URL https://aip.scitation.org/doi/abs/10.1063/1.2432410.

Acronyms

F_N normal force.

AC alternating current.

AFM atomic force microscope or atomic force microscopy.

AM-AFM amplitud modulated dynamic scanning force microscopy.

CP contact potencial.

CPD contact potential difference.

DC direct current.

DSFM dynamic scanning force microscopy.

EAFM electrostatic atomic force microscopy.

ESFM electrostatic scanning force microscopy.

ESFM2 electrostatic scanning force microscopy at 2 nu.

FM-AFM frequency modulated dynamic scanning force microscopy.

FM-DSFM frequency modulated dynamic scanning force microscopy.

HOPG highly oriented pyrolytic graphite.

KPFM Kelvin probe force microscopy.

KPM Kelvin probe microscopy.

MFM magnetic force microscopy.

PhM-AFM phase modulated dynamic scanning force microscopy.

PLL phase-locked loop.

STM scanning tunneling microscope.

Glossary

capillary bridge Minimized surface of liquid created between two rigid bodies with an arbitrary shape. plural. 43, 52

interaction image An AFM technique based on the measurement of tip-sample interaction not only as a function of tip-sample distance, but also as a function of tip-sample voltage. plural. 54